International Journal of Non–Linear Mechanics 175 (2025) 105098

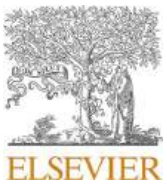

Contents lists available at ScienceDirect

International Journal of Non-Linear Mechanics

journal homepage: www.elsevier.com/locate/nlm

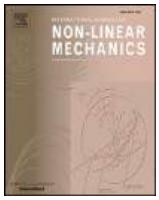

Chaotic dynamics of spiral bevel gears

Moslem Molaie [a], Antonio Zippo [b], Francesco Pellicano [b,*]

[a] Department of Engineering "Enzo Ferrari", University of Modena and Reggio Emilia, Modena, Italy
[b] Department of Engineering "Enzo Ferrari", Centre InterMech MoRe, University of Modena and Reggio Emilia, Modena, Italy

ARTICLE INFO

Keywords:
Non-smooth dynamical system
Nonlinear mesh stiffness
Hertzian contact stress
Nonlinear times series analyses
Chaos analyses
Recurrence quantification analyses

ABSTRACT

This study investigated the nonlinear dynamics of a Spiral Bevel Gear (SBG) system used in helicopter transmissions. Two approaches were employed to determine the Mesh Stiffness (MS): the average slope method (average-MS) and a hybrid analytical-computational method (adaptive-MS), which accounts for Hertzian contact nonlinearity. The dynamic mesh force was computed using polynomial interpolation techniques and loaded tooth contact analysis. The accuracy of the adaptive-MS approach was validated through comparison with a verified nonlinear finite element method (Nonlinear-FEM) simulation, demonstrating strong agreement. The GearDyns-SBG program was used to solve the system's dynamic model under varying working conditions. Backward and forward simulations were conducted to track stable branches, providing insights into the system's behavior. The study evaluated the dynamic responses based on both mesh stiffness approaches using tools such as FFT spectrum, amplitude-frequency analysis, nonlinear time series analysis, Poincaré maps, phase diagrams, and recurrence plots. The results revealed complex behaviors, including tooth separation, backside contact, boundary crises, and period-doubling cascades. Additionally, the largest Lyapunov exponent and fractal dimension were used to characterize the dynamics and 3D bifurcation analysis captured transitions between regular and chaotic regimes. The periodicity characteristics of the system were evaluated by recurrence quantification analyses. These findings enhance the understanding of nonlinear gear dynamics of SBG and provide reliable methods for predicting and analyzing their behavior.

1. Introduction

Gear transmission power systems embrace a diverse range of engineering applications, including aerospace, industrial machinery, and transportation systems. In specific scenarios, such as the interior of helicopter cabins, noise reduction becomes a critical consideration. Within these contexts, the gears in transmission system often emerge as primary noise sources. Flight tests have revealed that planetary gear trains and spiral bevel gear sets (SBG-sets) are significant contributors to transmission vibration [1]. Furthermore, reliability is a crucial aspect in the design of these applications, which are influenced by system vibrations. Consequently, a thorough analysis of the gear dynamics is essential for accurately predicting system behavior and mitigating negative effects of vibrations on durability.

Although gear vibrations and dynamics have been extensively studied in recent years, reliable nonlinear models are not so common and commercial software are still far from acceptable performances. Conventional methods often rely on simplifications, such as ignoring the effects of Hertzian stress and thus neglecting the nonlinearity of mesh stiffness (MS) due to applied torque [2]. Typically, MS is treated as a time-varying parameter, expressed through Fourier series [3–7] or sinusoidal functions [8–10]. In 2013, Eritenel and Parker [11] introduced a model incorporating a force-deflection curve to account for partial contact loss. Partial contact loss occurs when segments of the contact line lose contact, while others remain engaged. This model utilized a lumped-parameter approach with a single degree of freedom (SDOF). The MS decreases as partial contact is lost due to reductions in profile and face contact ratios caused by the vibration; however, contact is sustained. During partial contact loss, nominal contact lines may disconnect even though the gear teeth remain engaged. This phenomenon is particularly evident in systems with tooth profile and lead modifications. Quadratic and cubic nonlinearities effectively represent the nonlinearity arising from partial contact loss in modified gears, significantly influencing the nonlinear response. Cooley et al. [12] compared two methodologies for MS calculation: the local slope approach (which considers the nonlinear MS affected by Hertzian stress) and the average

This article is part of a special issue entitled: Nonlinear Vibrations published in International Journal of Non-Linear Mechanics.

* Corresponding author.
E-mail addresses: moslem_molaie@unimore.it (M. Molaie), antonio.zippo@unimore.it (A. Zippo), francesco.pellicano@unimore.it (F. Pellicano).

https://doi.org/10.1016/j.ijnonlinmec.2025.105098
Received 3 September 2024; Received in revised form 10 March 2025; Accepted 24 March 2025
Available online 4 April 2025

slope method (a conventional approach). They demonstrated that the average slope method is suitable for static analyses, whereas the local slope method is more appropriate for dynamic analyses of gears vibrating around a nominal static deflection. Their findings indicated that the local slope approach predicts higher stiffness values than the average slope approach throughout the mesh cycle. In 2019, Dai et al. [2]. developed a model to evaluate the dynamic response of an SBG-system by employing a force-deflection curve to predict dynamic mesh forces (DMF). They applied both the average slope approach and the local slope approach to determine MS and DMF. Additionally, they interpolated the dynamic mesh force from the force-deflection curve using the LS-SVMlab toolbox [13], applying the same interpolation function for forward and backside contacts. Their study concluded that the local tangent mesh stiffness approach is preferable for analyzing gear vibrations around nominal static deformations, as it better captures the relationship between dynamic mesh force and nominal static mesh force.

The comprehension of system dynamics relies on observation, measurement, analysis, and, where possible, prediction of behaviors observable in nature. Linear or near-linear systems exhibit regularity and operate under stable conditions, making them accessible to traditional technical investigations. However, many systems exhibit complexities that are inherently nonlinear and sometimes unpredictable. Thus, specialized tools are necessary to evaluate and predict their dynamic responses. These tools include spectral kurtosis [14], recurrence plots (RPs) and recurrence quantification analysis (RQA) [15], bifurcation analyses, nonlinear time series analyses, spectrum analyses [16,17]. The data analysis tools like bifurcation diagrams, Poincaré maps, phase portraits and spectra, find applications also in experimental data coming from different mechanical systems, see Refs. [18,19]. Recurrence plots (RPs) visualize the behavior of trajectories in phase space. The recurrence quantification analysis (RQA) then quantifies structures found in RPs to yield objective measures of such patterns [20] and are widely applied in different fields, e.g., climatological data [21], radiocarbon data [22], systems with white noise [23]. In this study, we apply such data analysis tools to understand the dynamic properties of a helicopter transmission system [17]. The aforementioned advanced techniques are accompanied by traditional spectra analyses; indeed, for systems exhibiting regular responses, the spectrum shows a series of peaks at discrete frequencies, i.e., excitation frequencies; the spectrum reveals the dynamic characteristics of non-periodic motion, e.g., amplitude modulation, frequency modulation, phase modulation, and pulse width modulation; in such cases one deserves sidebands with different spacing [16,24]. When dealing with complex nonlinear dynamical systems, further data analysis techniques could be used to analyze the system's response and reveal intimate nature. Nonlinear time series analysis is particularly useful in this regard, providing parameters such as fractal dimension [16,25] and largest Lyapunov exponent (LLE) [16,26], which aid in identifying system attractors and understanding the system's behavior more comprehensively.

In the present study, we investigate a real SBG-pair considered in a helicopter power transmission to investigate the performances of two methods for obtaining mesh stiffness: the average slope approach (average-MS) and a hybrid analytical-computational approach (adaptive-MS), which accounts for nonlinearity due to Hertzian contact stress. For the latter one, the DMF is computed using a combination of polynomial interpolation techniques and loaded tooth contact analyses. The accuracy of the adaptive-MS is assessed by comparing its results with those from a verified Nonlinear-FEM simulation. The dynamical system considered is non-smooth and non-autonomous due to the presence of backlash, nonlinear, time-varying mesh stiffness and torque. We analyze and compare the dynamic responses of two systems, each one using the aforementioned mesh stiffness methods, to understand differences and inaccuracies. Different tools are considered to analyze the dynamics: nonlinear time series analysis for evaluating the largest Lyapunov exponent and fractal dimension, 2D and 3D bifurcation diagrams, amplitude-frequency analyses, Poincaré maps, phase diagrams, recurrence plots, recurrence quantification analysis, and spectrum analysis. In the final part of this study, we investigate the system response under low torque levels.

2. Mesh stiffness analysis

Fig. 1 depicts a schematic of a spiral bevel gear system, illustrating the power transmission between two perpendicular axes. The analysis employs a purely torsional dynamic model, where all translational degrees of freedom (DOFs) are restricted, allowing both the gear and the pinion to rotate exclusively around their respective axes.

Mesh stiffness (MS) is a key parameter when it comes to dynamics of a transmission system. Indeed, to analyze the dynamic behavior of the system using analytical lamped parameter models, it is essential to obtain MS in advance. Loaded static transmission error (LSTE) is the parameter which used to define MS as [27]:

$$k = \frac{T}{r_b}\left[\frac{1}{LSTE - e}\right] \tag{1}$$

Where, T/r_b is the force felt by mated teeth of the pinion and the gear, and $(LSTE - e)$ is the elastic deflection of the tooth under the applied force. It is important to note that such a force is not always the input force, although many studies have been conducted based on this assumption. Initially, the force applied to the mated teeth equals the input force; however, after that, the two mated teeth experience the DMF which is influenced by inertial forces. When solving the governing equations, DMF varies at each time step due to vibrations, or more precisely, to the dynamic transmission error (DTE) fluctuation. Another key point is that the relationship between force and deflection is nonlinear because of the Hertzian contact stress. In traditional dynamic models, the nonlinearity due to Hertzian contact stress is often ignored, and a linear function is used. Additionally, the applied force is assumed to be equal to the input force.

Figs. 2 and 3 illustrate the torque-torsional deflection curve for forward and reverse directions of motion, respectively. In these figures, torque is applied to the gear, and the mean value of torsional deflection is considered for representing the results. To obtain these results, more than 830 semi-static simulations were performed using a nonlinear finite element software, Transmission3D-Calyx®; a MATLAB code was written to run the software, extract the results, update the input torque, and repeat the procedure. By comparing Figs. 2 and 3, it can be concluded that the effect of nonlinearity is dependent on the geometry of the gear pair. Another point worth mentioning is that, in the case considered, nonlinearity significantly influences the system's dynamics when the dynamic mesh torque (DMT) is in the range of 0–1000 N•m. In the initial region of the curve, the behavior is primarily governed by Hertzian elasticity, resulting in a markedly nonlinear response. This nonlinearity

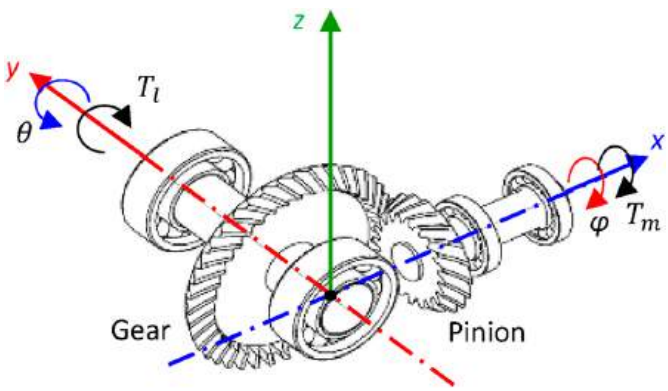

Fig. 1. The dynamic model of the gear system with torsional-DOF.

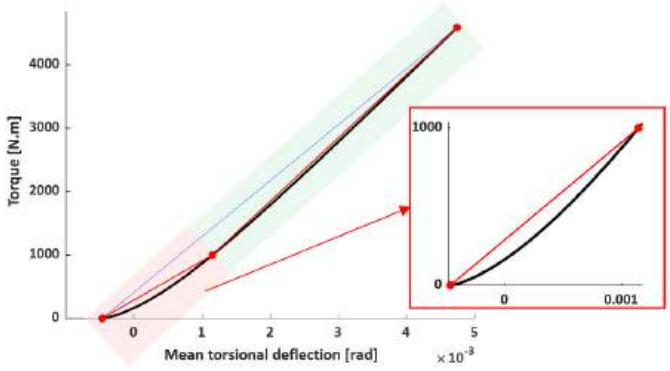

Fig. 2. Torque (on the gear) vs mean torsional deflection extracted from semi-static simulations in the forward direction of motion.

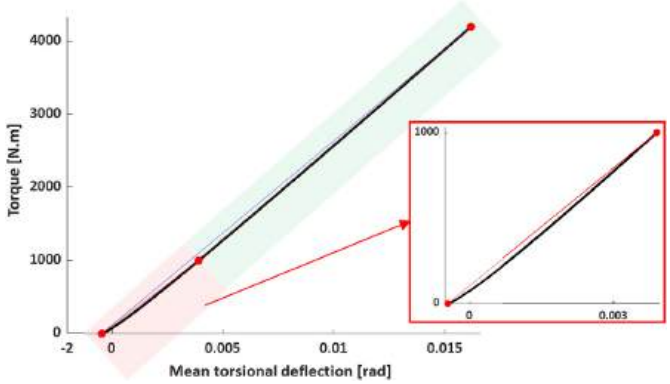

Fig. 3. Torque (on the gear) vs mean torsional deflection extracted from semi-static simulations in the reverse direction of motion.

diminishes in the later stages as elastic contributions become more prominent. Near the origin, the local stiffness is relatively lower, emphasizing the impact of Hertzian effects. Additionally, the nonsymmetric geometry of spiral bevel gears introduces a significant disparity between forward and backward stiffness, highlighting the complexity of the gear's mechanical response under varying load directions.

2.1. Mesh stiffness calculation in terms of DMT dependency: novel approach

Different studies have been conducted to determine models for MS calculation, such as the average slope approach and the local slope approach [12,28,29]. In this study, an adaptive approach is proposed to obtain accurate MS at each time step. The proposed model is based on semi-static simulations conducted using a nonlinear FEM, Transmission3D-Calyx®, then the results are interpolated through polynomial regression. The nonlinear FEM analysis was validated, in Refs. [16,17]. A polynomial function with degree $n = 9$ is utilized for interpolating the cloud of numerical data. The first step for MS calculation is to obtain the torsional elastic deflections in order to calculate it at a specific time, a semi-static simulation is carried out, where the inner diameter of the gear is considered fixed, and torque is applied to the pinion. Over time, the teeth of the pinion and the gear come into and leave contact, resulting in changes in the position of the mated teeth; consequently, the static simulation must be repeated at different time steps.

In this study, we consider 21 timesteps during which two teeth come into contact and then separate, moreover the contact point continuously changes during the gear rotation; see e.g. Fig. 4 where step No. 1 is the initial contact between two teeth and step No. 21 indicates when the contact between the teeth is lost. For the intermediate steps the contact

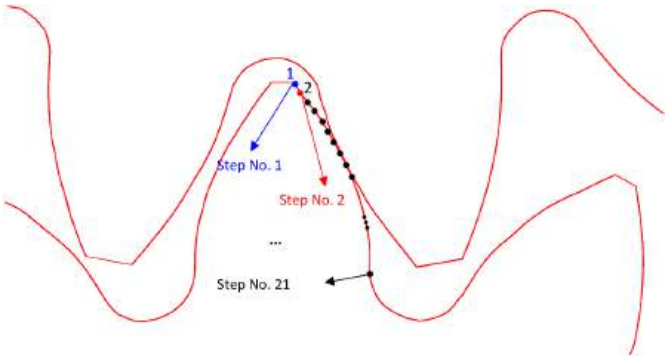

Fig. 4. Mated two teeth of the pinion and the gear with the time-step schematics.

force changes position and stresses the tooth with different bending moments, so the overall deflection continuously varies. Results of semi-static simulations are shown in Figs. 6 and 7 which depict the torsional deflection of the gear pair under different ranges of applied torque on the gear during forward and reverse directions of motion, respectively. In order to develop a dynamical model, it is necessary to have the torsional deflection as a continues function of time; therefore, a polynomial function with degree $n = 9$ is employed to fit on the results extracted from FEA at each 21-timesteps.

$$f(x_i) = a_1{*}x_i^{\,9} + a_2{*}x_i^{\,8} + a_3{*}x_i^{\,7} + a_4{*}x_i^{\,6} + a_5{*}x_i^{\,5} + a_6{*}x_i^{\,4} + a_7{*}x_i^{\,3} + a_8{*}x_i^{\,2} + a_9{*}x_i + a_{10} \quad (2)$$

Eq. (2) represents the fitted curve at i-step, where x_i is the dynamic mesh torque. This point has to be considered that steps 1 and 21 provide us with the same results. For the first 8 timesteps, the fitted curve and the numerical FEA results are shown in Figs. 6 and 7 for the forward and the reverse direction of motions respectively. Table 8 and Tables 9 and in Appendix C, present the polynomial coefficients for 21 timesteps during forward and reverse direction of motions respectively. For the forward motion, Fig. 6, the nonlinearity takes place next to the origin due to the Hertzian deflection; while, in the straight part of the curve (linear zone) is not greatly affected by the position, i.e., the deflection of STE is smaller for medium-high loads. The nonlinear zone varies with the position, giving rise to a fluctuation of the nonlinear part of the stiffness. On the other hand, for the reverse direction of motion, i.e., Fig. 7, the torque-deflection curve is almost linear and experiences a linear fluctuation.

To calculate the MS of the system besides the LSTE, the geometric transmission system (GTE) is required to obtain from unloaded tooth contact analysis (UTCA), see Fig. 5. To conduct the UTCA, a negligible eligible torque (0.001 N · m) is applied on the gear.

By obtaining LTSE and GTE, Eq. (1) is used to calculate the mesh stiffness of the system as the function of both time and displacement, this allows to update the mesh stiffness based on the DMT and time and then solve the governing equation of motion.

2.2. Validation of adaptive mesh stiffness interpolating function

To assess how much is accurate the interpolation, we examined the torsional deflection when 537 N·m of torque was applied to the gear in the forward direction. Fig. 8 shows the torsional deflection of the SBG obtained by FEA (red line) vs. the interpolating function represented by the blue line. A small discrepancy between the two scenarios is observed at time step number 8, with a difference of 2.4 %. Considering the average torsional deflection values for both methods, the overall difference between the two curves reduces to 1.7 %. Thus, we can conclude that the interpolation offers remarkable accuracy, making it suitable for mesh stiffness calculation during dynamic simulations where updates to the mesh stiffness must be a continues function of time and

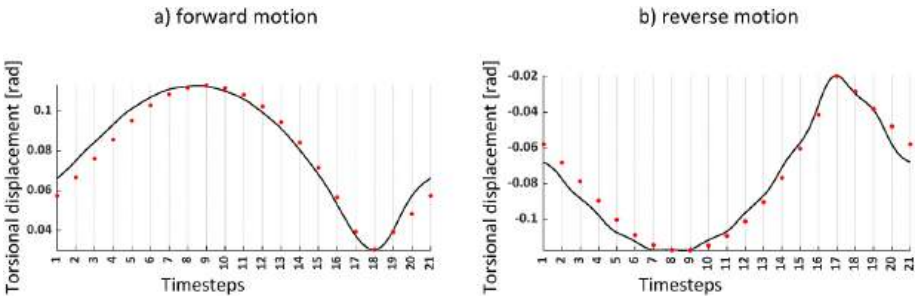

Fig. 5. Rigid body transmission error (the gear rotation) – UTCA: torque 0.001 N · m: a) forward motion, b) reverse motion; ▬ Fitted curve, ● FEM results.

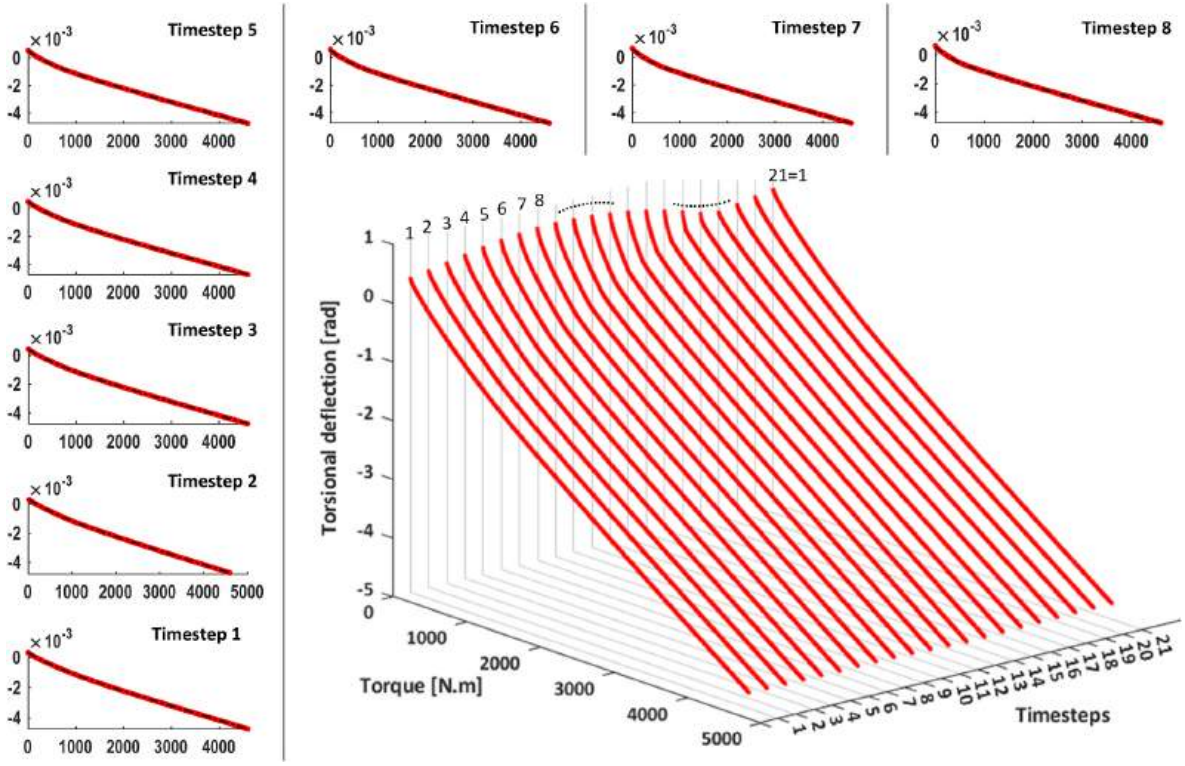

Fig. 6. Force-deflection function obtained by finite element analysis of the SBG with increasing applied torque in forward motion.

displacement.

It is essential to highlight that the FEA results have been validated with experimental data and FEM in a previous study conducted by Molaie et al. [17]. Fig. 9 provides a comparison between experimental results [30] and the FEM results [31]: the red line represents the root stress for the pinion tooth derived from experimental data [30] while the black line represents the root stress extracted from the finite element simulation [17]. The comparison demonstrates excellent agreement between the two. For reference, the numerical simulation is done by Bibel et al. [31]: who conducted a nonlinear FEM analysis using MSC Marc to simulate the gear pair defined in Appendix A. Their simulation focused on a model with three pinion teeth and four gear teeth, with the pinion fixed in place and the gear restricted to rotation around its axis [31].

2.3. Proposed approach for mesh stiffness calculation in terms of time dependency

When addressing the changes in mesh stiffness over time at a specific dynamic mesh torque, it necessitates a periodic function to express its variation as time progresses. One commonly employed function to represent the MS of the system is the Fourier series, which incorporates the mesh frequency, $\omega_m = \frac{2\pi}{60} N_p n_s$, where n_s is the input shaft speed and N_p is the number of pinion teeth; the equivalent meshing stiffness is given by:

$$K_m(t) = k_0 + \sum_{j=1}^{S} a_j \cos(j\omega_m t) + \sum_{j=1}^{S} b_j \sin(j\omega_m t) \tag{3}$$

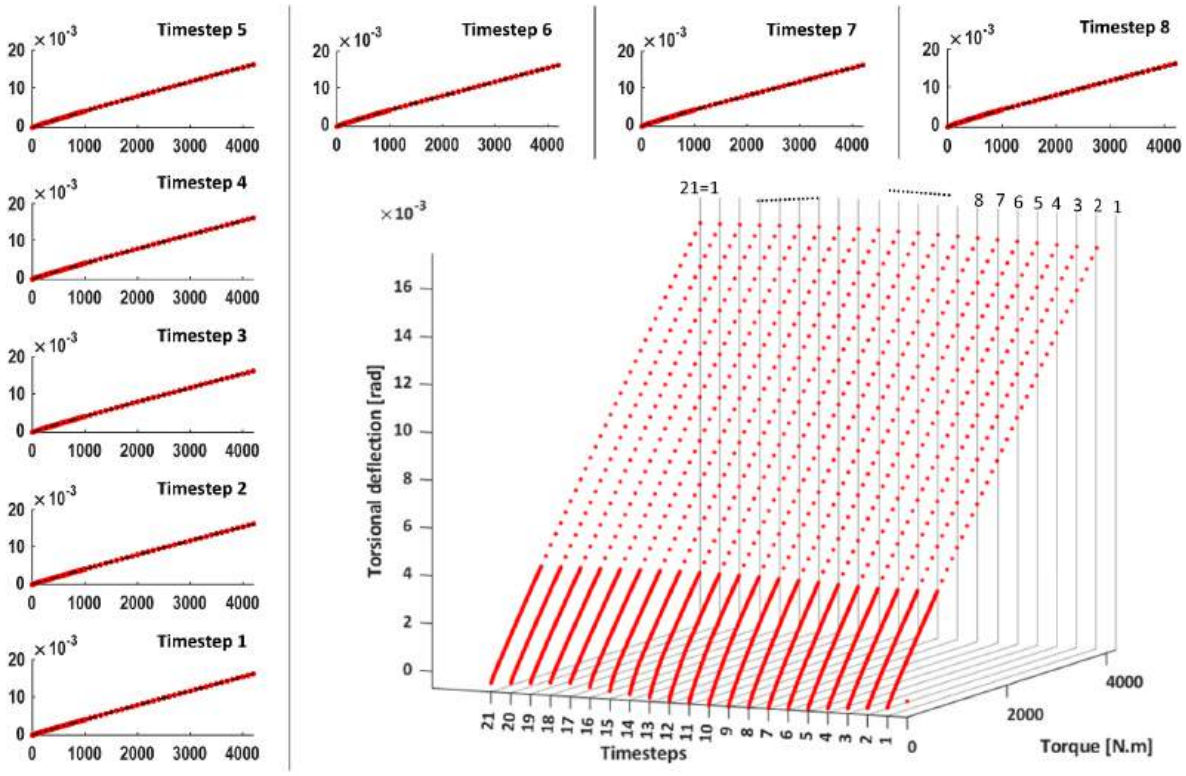

Fig. 7. Force-deflection function obtained by finite element analysis of the SBG with increasing applied torque in reverse motion.

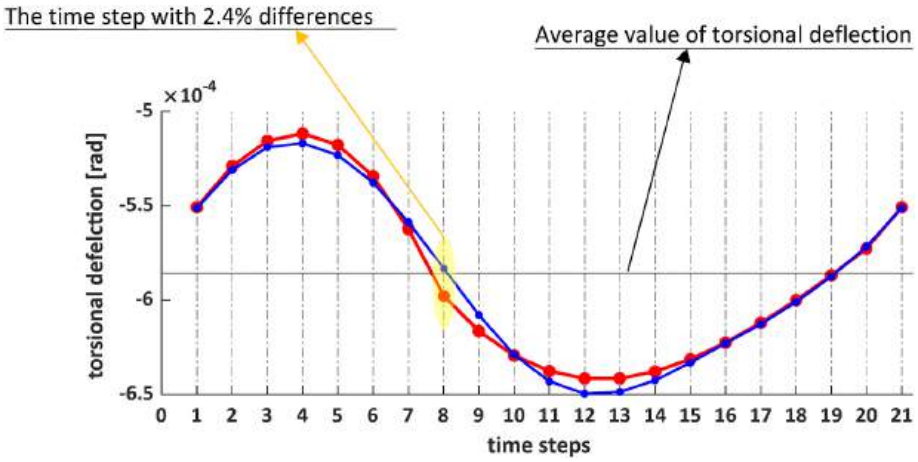

Fig. 8. Torsional deflection of two methods at torque equals 537 N·m:
extracted from FEM analysis, obtained from presented method.

Where, s is the number of harmonics of Fourier series and obtains by $s = (N_1 - 1)/2$. N_1 is the number of time steps that is used to provide the torsional deflection started from one tooth comes to contact and leave the contact.

3. Dynamics analysis

In this study, an SDOF system is used to analyze the effect of nonlinear mesh stiffness on the dynamic behavior of the gear system—an aspect often neglected in conventional gear transmission analyses due to the significant complexity it introduces into the system's dynamics. Additionally, considering the effects of other components, such as lateral vibrations from bearing characteristics, led to results that, when combined with the current findings, produced complex and difficult-to-interpret outcomes. The following assumptions are made: the contact is assumed to be dry and frictionless, thermal effects are neglected, multimesh systems are not considered, and lateral vibrations arising from bearings and shafts are disregarded. The governing equations of motion are derived for the system with single degree of freedom, shown in Fig. 10.

The dynamic equations of motion in "θ" and "φ" direction for the gear (θ_g) and pinion (φ_p) are:

$$I_g^{x}\ddot{\theta}_g = -r_g F_z - T_l \tag{4}$$

$$I_p^{x}\ddot{\varphi}_p = r_p F_z + T_m \tag{5}$$

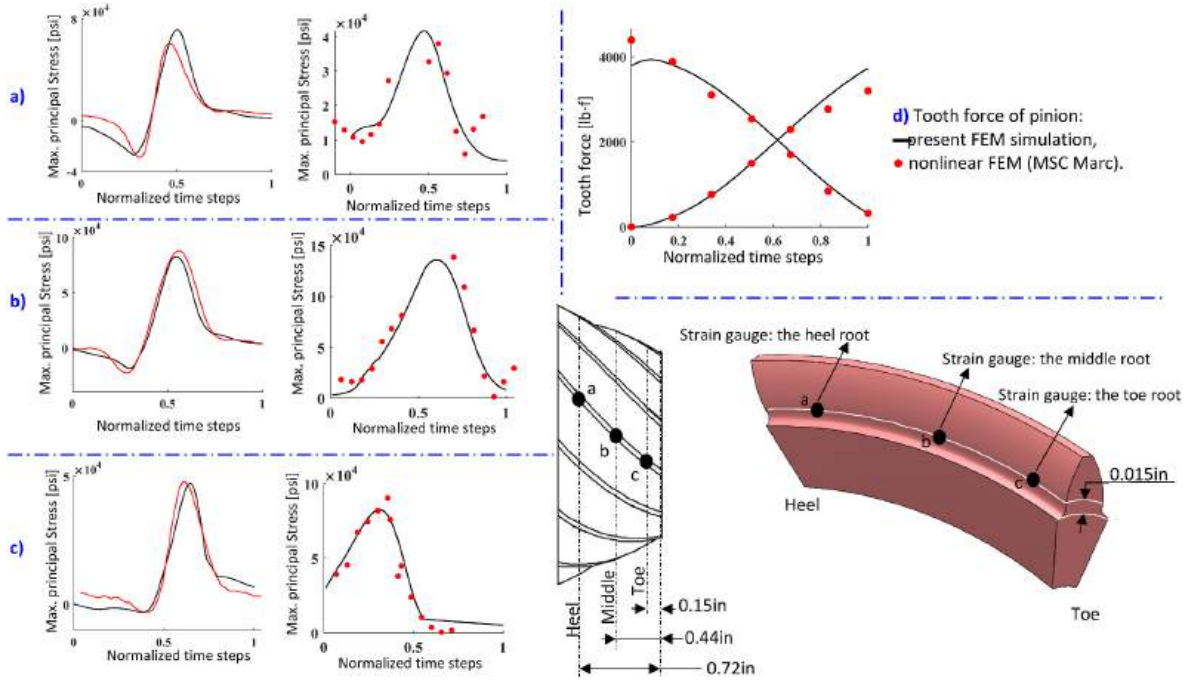

Fig. 9. Maximum principal stress on the root of the tooth respect to pinion for a) the heel root, b) the middle root, c) the toe root, and d) tooth force ▬ FEM (Transmission3D-Calyx) simulation [16], ▬ Experimental results [27], ● FEM (MSC Marc) [28].

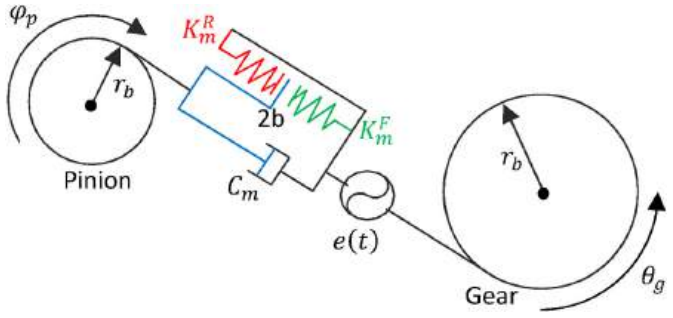

Fig. 10. Torsional dynamic model of the gear system with SDOF.

Local imperfection between mating teeth may arise due to mounting issues, manufacturing errors (Fig. 12), or intentional modifications to the teeth profile. This phenomenon is referred to as geometric transmission error (GTE), see Fig. 11. In this study, GTE is calculated using a UTCA for both forward and reverse motions, denoted as $e^F(t)$ and $e^R(t)$ respectively:(see Fig. 13)

$$e(t)=\begin{cases} e^F(t)=e_0^F+\sum_{j=1}^{s} ea_j^F\cos(j\omega_m t)+\sum_{j=1}^{s} ea_j^F\sin(j\omega_m t) & \text{forward motion} \\ e^R(t)=e_0^R+\sum_{j=1}^{s} ea_j^R\cos(j\omega_m t)+\sum_{j=1}^{s} ea_j^R\sin(j\omega_m t) & \text{reverse motion} \end{cases} \tag{6}$$

The linear dynamic transmission error (DTE), λ, along the line of action is defined as:

$$\lambda=(r_p\varphi_p-r_g\theta_g)a \tag{7}$$

where, $a = \cos\alpha\times\cos\beta$, β is the spiral angle and α is the normal pressure angle.

The dynamic load of pinion and its component along the line of action is F_n and along the z- axis is F_z which are defined as:

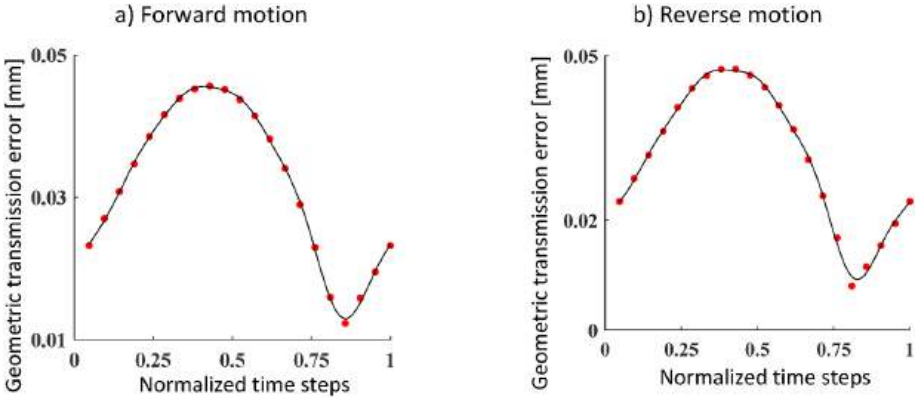

Fig. 11. Geometric transmission error on the line of action [17]: a) forward motion, b) reverse motion; ▬ Fitted curve by Fourier series, ● FEM results.

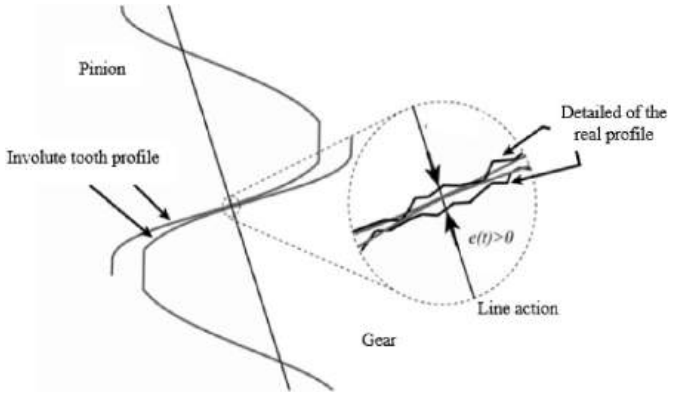

Fig. 12. Geometric transmission error: lack of material along the line of action [16].

$$F_z=-F_n a;\ F_n=C_m(\dot{\lambda}-\dot{e})+K_m f(\lambda-e);\ f(\lambda-e)=\begin{cases}\lambda-b-e, & \lambda-e>b\\ 0, & -b\le\lambda-e\le b\\ \lambda+b-e, & \lambda-e<-b\end{cases} \tag{8}$$

In (8) the nominal force is given by a linear and an elastic nonlinear term, where:

$$K_m(t)=\begin{cases}K_m^F, & \lambda-e>b\\ K_m^R, & \lambda-e<-b\end{cases} \tag{9}$$

The backlash function, denoted as $f(\lambda-e)$, is a piecewise linear function described in Eq. (9). When this function is multiplied by the stiffness, it produces the elastic restoring force [32]. If the value of $\lambda-e$ lies within the range $-b$ to $+b$, it indicates a loss of contact between the teeth, which is an undesirable situation [33,34]. Ideally, when $\lambda-e>b$, the gear teeth are in forward contact, which is the desired scenario, and the stiffness, K_m^F, is determined from static nonlinear finite element analysis (FEA) during this forward motion. However, if $\lambda-e<-b$, the teeth experience unwanted backside contact, leading to a double-sided impact, where the stiffness, K_m^R, is derived from static simulations during reverse motion [33]. Experimental findings in Ref. [35] suggest that tooth separation is likely, indicating the importance of considering gear backlash non-linearity in dynamic models. Additionally, these findings highlight that fluctuations in mesh stiffness are a major source of excitation within the gear system and must be included in the governing equations to accurately model the gear dynamics.

In order to normalize the governing equation, the following parameters are introduced.

$$\tau=\omega_n t\quad \bar{\lambda}=(\bar{r}_p\varphi_p-\bar{r}_g\theta_g)a_3\quad \ddot{\theta}=\omega_n^2\theta''\quad \dot{\theta}=\omega_n\theta'$$
$$\bar{r}_p=r_p/b\qquad \bar{r}_g=r_g/b\qquad \ddot{\varphi}=\omega_n^2\varphi''\quad \dot{\varphi}=\omega_n\varphi' \tag{10}$$

$$\overline{T}_{eq}=\frac{1}{bm_{eq}\omega_n^2}\left(\frac{T_m}{r_p a_3}\right)\quad \omega_n=\sqrt{K_0/m_{eq}} \tag{11}$$

$$\xi=\frac{C_m}{2m_{eq}\omega_n}\quad m_{eq}=\left(\frac{(r_p a)^2}{I_p^x}+\frac{(r_g a)^2}{I_g^y}\right)^{-1} \tag{12}$$

Consequently, Eqs. (4) and (5) can be rewritten as follows [3,5]:

$$\bar{\lambda}''+\overline{K}_m f(\bar{\lambda}-\bar{e})+2\xi\bar{\lambda}'=\overline{T}_{eq} \tag{13}$$

where,

$$f(\bar{\lambda}-\bar{e})=\begin{cases}\bar{\lambda}-\bar{e}-1, & \bar{\lambda}-\bar{e}>1\\ 0, & -1\le\bar{\lambda}-\bar{e}\le 1\\ \bar{\lambda}-\bar{e}+1, & \bar{\lambda}-\bar{e}<-1\end{cases} \tag{14}$$

$$\overline{K}_m(t)=1+\sum_{j=1}^{S}\frac{a_j}{m_{eq}{\omega_n}^2}\cos(j\omega_m t)+\sum_{j=1}^{S}\frac{b_j}{m_{eq}{\omega_n}^2}\sin(j\omega_m t) \tag{15}$$

3.1. Mesh stiffness, K_m

One of the main goals of this study is to reveal the effect of Hertzian stress on dynamics of the system so that a comparison is carried out between a case with average time varying MS and adaptive MS. For this reason, here in this section two different functions are represented to define the MS of the SBG-system.

a) a periodic function over time, see Eq. (17): $K_m(t)$, expressed by Eq. (3), stiffness is only time dependent
b) a periodic function over time that is updated at each step of time based also on the new DMT, indeed the K_m is time and deflection dependent, see Eq. (18): $K_m(DMT,t)$, where:

$$DMT=F_n\cdot r_b \tag{16}$$

$$K_m(t)=\begin{cases}K_m^F(t), & \lambda-e>b\\ K_m^R(t), & \lambda-e<-b\end{cases} \tag{17}$$

$$K_m(DMT,t)=\begin{cases}K_m^F(DMT,t), & \lambda-e>b\\ K_m^R(DMT,t), & \lambda-e<-b\end{cases} \tag{18}$$

The procedure of average MS consideration is well explained in many papers, see Refs. [7,16,17] (see Fig. 14). To clarify the adaptive

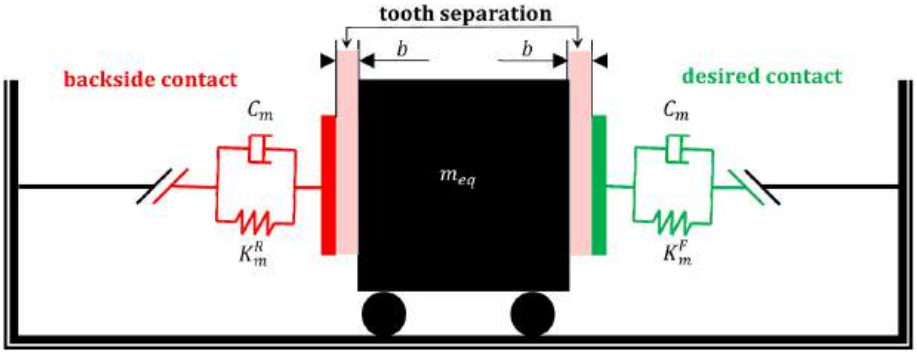

Fig. 13. Equivalent gear model and backlash function.

MS consideration, an algorithm is presented in Fig. 15.

4. Numerical results

The governing equation, Eq. (13), is a non-smooth and non-autonomous dynamical system where the system is excited parametrically in addition to the external torque (transmitted power). A program, GearDyns-SBG, is designed by FORTRAN language to solve numerically the equation based on an implicit fifth order Runge-Kutta scheme (RADAU). GearDyns-SBG has the ability to carry out chaos and bifurcation analyses to delve into the dynamic behavior of the SBG-system. The used algorithm in the program is extremely stable and accurate, see e.g. Refs. [3,5–7,16,17,32].

GearDyns-SBG calculates the time responses by direct simulation to construct the amplitude–frequency diagram and the bifurcation diagram of Poincaré maps, obtained by varying the excitation frequency, i.e., the pinion rotation speed. From a theoretical standpoint, different solutions to the governing equation can exist; however, some solutions are practically infeasible and cannot be physically achieved. The transitions occurring near the jumps are not recorded. Therefore, the simulation is conducted based on two different concepts: a) backward simulation, where the rotation speed starts from the highest to the lowest value (from high to low excitation frequency), and b) forward simulation, from low to high speed or excitation frequency. The backward simulation completes the analysis, allowing the tracking of all stable branches, particularly the softening branches, which are almost completely followed. During each simulation, the transient phase is separated from the "steady-state" for each frequency; the first 1000 periods are considered transient, and beyond that, the influence of frequency variation is assumed to be expired. GearDyns-SBG provides various diagrams such as 2D/3D Poincaré maps, 2D/3D phase portraits, time-history plots, 2D/3D bifurcation diagrams, and FFT spectra. Each Poincaré map is obtained by sampling the time histories with the same period as the meshing frequency. All necessary data for dynamic simulation and SBG properties are given in Appendix.

4.1. Nominal working condition

Analyzing the amplitude-frequency diagram is mainly the first step of investigating the dynamic response of the system. As shown in Fig. 16-a, to represent the amplitude-frequency diagram, the root-mean-square (rms) of the nondimensional dynamic transmission error ($\bar{\lambda}$) is used over nondimensional excitation frequency (ω_m/ω_n) with the range of [0.1, 3.5], and $T_m = 179$ N·m. To find out the reason of some phenomena, which appear on the amplitude-frequency diagram, it is recommended to use the bifurcation diagram besides to the amplitude-frequency diagram, see Fig. 16-b and Fig. 16-c. To represent better the dynamic behavior of the system, the extracted results are represented by different color:

- **Red dots** represent the dynamic response of the system associated with **average MS** approach. simulations are carried out for both increasing and decreasing the excitation frequency (**forward and backward simulations**).
- **Black dots** represent the dynamic response of the system associated with **adaptive MS** approach. Simulations are carried out while the excitation frequency is decreasing; **backward simulation: the rotation speed starts from the highest value to the lowest value.**
- **Blue dots** represent the dynamic response of the system associated with **adaptive MS** approach. Simulations are carried out while the excitation frequency is increasing; **forward simulation: the rotation speed starts from the lowest value to the highest value.**

There are some remarkable differences between average MS and adaptive MS. First of all, an undesirable backside contact appears in the dynamic response of the system where the average MS is used. Indeed, the small portion of a hardening branch is caught, due to very high vibration amplitudes when the backside contact takes place; the hardening branch takes place from $\frac{\omega_m}{\omega_n} = 0.463$ to $\frac{\omega_m}{\omega_n} = 0.495$. While in the system associated with the adaptive MS, there is not any trace of backside contact. The backside contact phenomenon might cause a rattling noise in the system. Clearances are inevitably required between the idle surfaces of engaging gear teeth in toothed connections to accommodate thermal expansion and manufacturing tolerances. When gears are lightly loaded with strongly oscillating torque and/or rotate at low speeds, there is a high possibility of meshing teeth separation or backside contact. This separation results in vibratory impacts between the teeth surfaces. The vibratory energy excitation within the working clearance generates annoying rattle noise [36]. Tooth separation appears as a softening branch while the double side impact or backside contact can be recognized by a hardening behavior in the dynamic responses of the system.

In general, there are three different resonances in a system: principal resonances of the higher super-harmonics of the time-varying stiffness

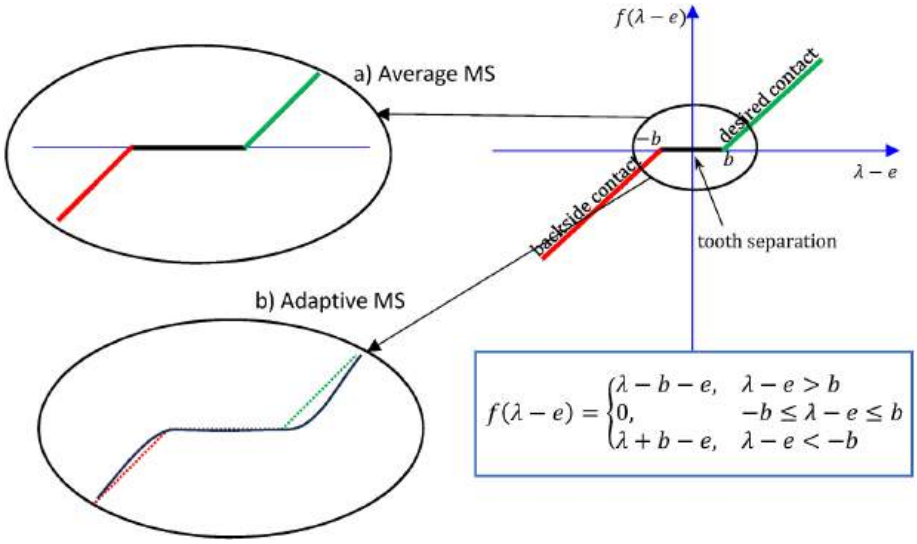

Fig. 14. Adaptive and average mesh stiffness representation.

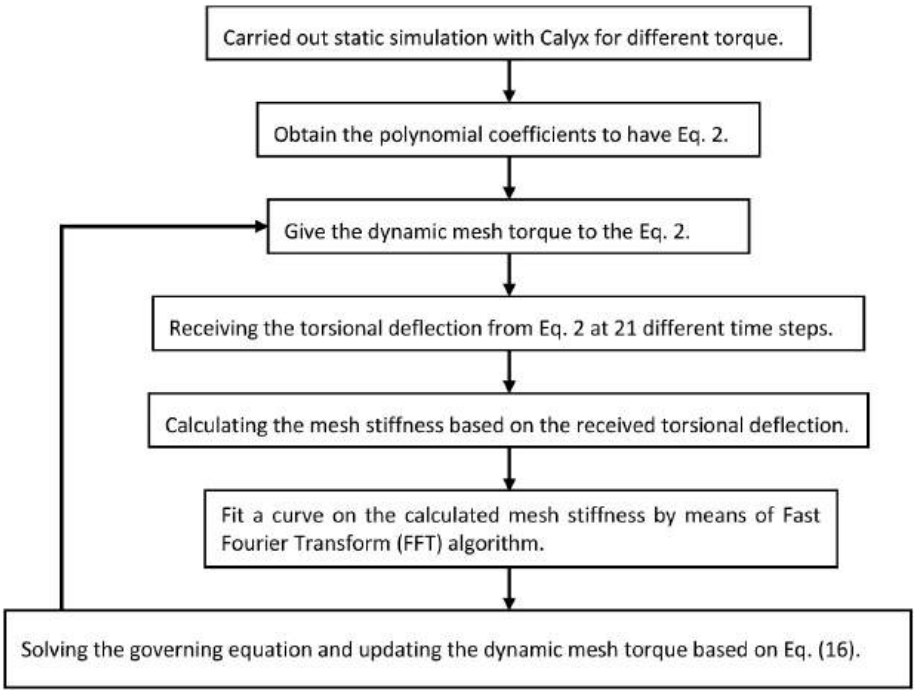

Fig. 15. The algorithm of adaptive mesh stiffness consideration.

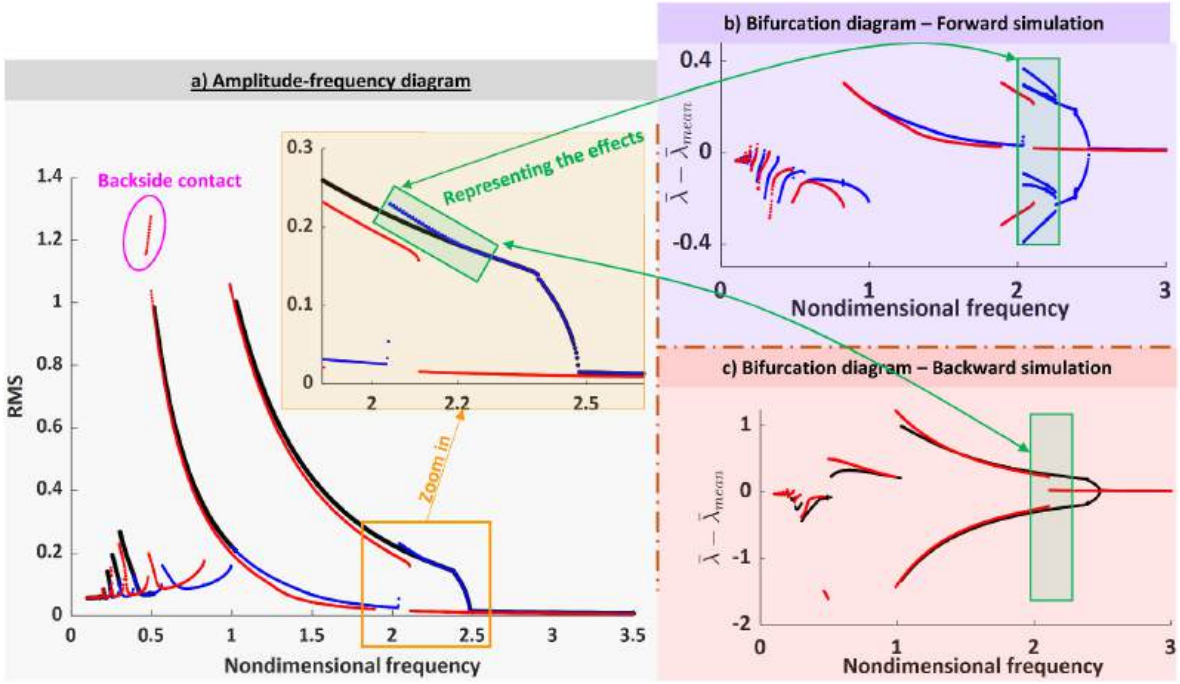

Fig. 16. Nonlinear dynamics of SBG for two different cases under nominal working condition; 1) adaptive MS, 2) average MS:
• Average MS approach obtained from forward and backward simulations, • Adaptive MS for backward simulation, • Adaptive MS for forward simulation.

presented at $\frac{\omega_m}{\omega_n} = \frac{1}{2}, \frac{1}{3}, \frac{1}{4}$, primary resonance due to the fundamental harmonic $\frac{\omega_m}{\omega_n} = 1$, and parametric resonance due to a strong sub-harmonic character presented at $\frac{\omega_m}{\omega_n} = 2$. At each of these excitation frequencies, it is supposed to have Resonance jump. The resonance branches show a softening character. Such softening behaviors are due to the loosing of contact that takes place when the inertia forces exceed the static contact force induced by the applied torque. A second visible difference between the two approaches, adaptive and average MS, backs to the dynamic behavior of the system where it experiences a sub-harmonic resonance at $\frac{\omega_m}{\omega_n} \approx 2$. The system related to the average MS approach shows a clear sharp jump, while the system employed the adaptive MS approach represents a smooth behavior. This behavior could be observed not only on amplitude-frequency diagram, Fig. 16-a, but also bifurcation diagram, Fig. 16-b and Fig. 16-c. Next point, that is interesting to mention, is the excitation frequency where two systems, developed by average and adaptive MS approaches, experienced the jumping phenomena. Indeed, there is a shift at excitation frequencies

where a resonance occurs in the system with adaptive MS consideration. These shifts stem from the parameter used to nondimensionalize the excitation frequency, which is the natural frequency, $\omega_n = 19714\ rad/s$, obtained from average MS approach. Based on the extracted results, shown in Fig. 16, the system associated with the adaptive MS is stiffer than the one associated with average MS approach.

The last interesting point regarding the dynamic results shown in Fig. 16 is the different path observed on dynamic response of the system associated with the adaptive MS for forward and backward simulations, see detailed view in Fig. 16-a. The reason behind this differences backs to the different behavior of the system observed in bifurcation diagram, see Fig. 16-b and Fig. 16-c. Indeed, the system in forward simulation has a 6T-periodic response, while in backward simulation has 2T-periodic behavior, so that the amplitude-frequency diagram shows a curve with a clear difference slope between the two types of simulation, in Fig. 16 two green arrows have been added to highlight with green rectangles the areas where we can observe this different behavior.

4.2. Low-level torque analysis

Gear rattling noise and gear whine noise are two primary NVH issues for automotive drivetrains such as in the transmission. The gear rattle noises in the powertrain and the drivetrain are related to torsional vibrations and torque fluctuation. The whine noise, another annoying gear noise, is excited by the transmission error at the gear mesh due to manufacturing errors and tooth deflection under load [36]. One of the working conditions that might cause gear whine noise in the system is working at high speed and low-level torque. For such reasons, in this section, we analyzed the dynamic response of the system at low level of torque, half of nominal applied torque on the pinion. The simulation is carried out at $T_m = 89.5$ N·m with the range of $\frac{\omega_m}{\omega_n} = [0.1\ 3.5]$.

The dynamic response of two systems (average and adaptive MS) are substantially different when the excitation frequency is varied in the high frequency ranges where the systems experience parametric resonance and sub-harmonic response. Fig. 17 clearly shows the nonlinear dynamic behavior of both systems under low-level torque conditions. The dynamic responses for all simulations, backward and forward, for both cases of average and adaptive MS, are represented in Fig. 17-a, while Fig. 17-b is the amplitude-frequency diagram for the average MS approach. The green color is dedicated to the results from the backward simulation where the average MS is considered, and the brown color is related to the same system but forward simulation. Besides, the black color is assigned to the adaptive MS method, backward simulation is carried out; the blue color defines the same system for forward simulation. Fig. 17-c and Fig. 17-d represent the bifurcation diagram of Poincaré maps for both methods at a specific range of nondimensional excitation frequency where a sub-harmonic resonance occurred in the system. As mentioned before, analyzing these two diagrams, amplitude-frequency and bifurcation diagrams, brings us a substantial insight into the systemic conditions.

Regardless of forward and backward simulation, the system where the adaptive MS is employed exhibits a chaotic behavior, while the system where we used the average MS experiences nT-periodic responses and in the worst scenario a double side impact. By considering the amplitude-frequency diagram, the aperiodic behavior is completely recognizable; however, the bifurcation diagram could show us the route to the chaos. Let's consider the excitation frequency range of $\frac{\omega_m}{\omega_n} = [1.8\ 2.8]$: the system developed by average MS experienced a jumping phenomenon due to the sub-harmonic resonance, conversely the system developed by adaptive MS represented a combination of softening, hardening and chaotic behavior that requires an in-detail investigation to comprehend better the system.

4.3. Dynamic investigation on the existence of the gear whine phenomenon

One of the remarkable differences between two approaches, average and adaptive MS, is the behavior of the system where the gear whine phenomenon occurred, see Fig. 17. The results approve that the nonlinear dynamic response of the system developed by average MS is mainly characterized by periodic to nT-periodic responses, while for the one based on the adaptive MS requires more investigation. To delve into

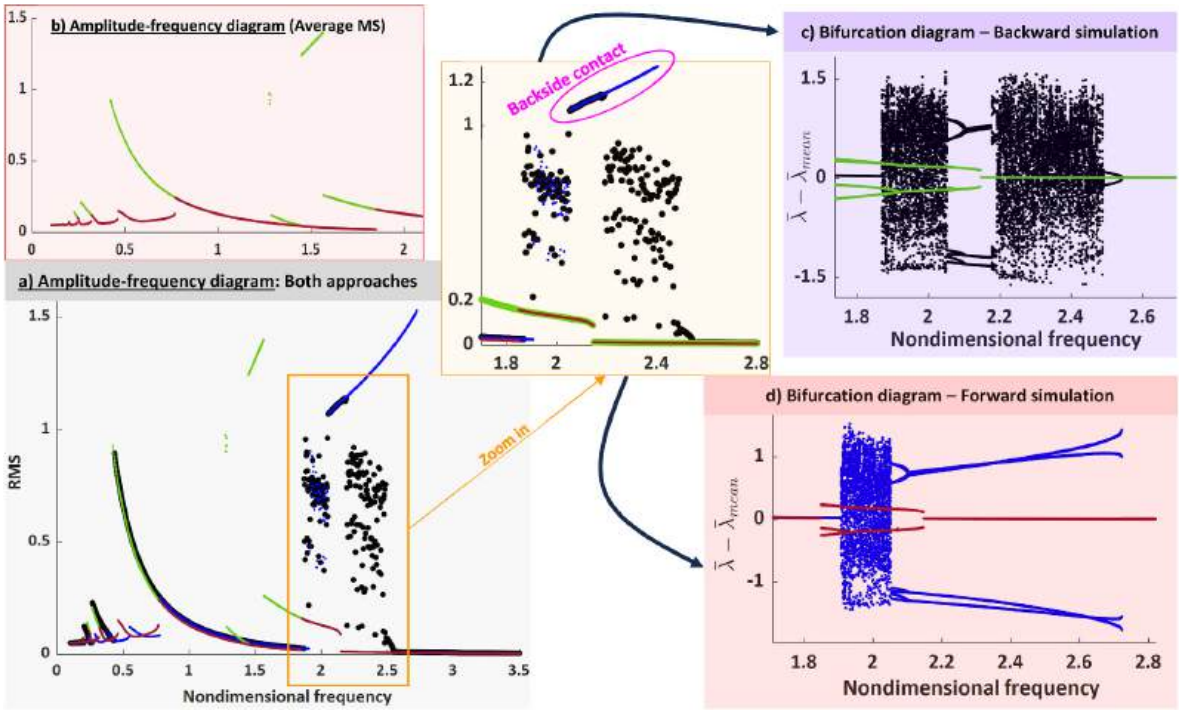

Fig. 17. Nonlinear dynamics of SBG for two different cases under low-level torque situation; 1) adaptive MS, 2) average MS: ● Average MS approach for backward simulation, ● Average MS approach for forward simulation, ● Adaptive MS for backward simulation, ● Adaptive MS for forward simulation.

the nonlinear vibration of the system where a hybrid analytical-computational approach (adaptive MS) is used, a 3D-bifurcation analysis is conducted. In Fig. 18, depending on the nonlinear dynamic behavior of the system, different colors are used to properly represent the dynamic response of the SBG. The frequency range is $\frac{\omega_m}{\omega_n} = [1.8\ 2.8]$.

Fig. 18-a shows the bifurcation diagram obtained from the backward simulation. By swing down the excitation frequency from $\frac{\omega_m}{\omega_n} = 2.8$, at the beginning, the system's response reveals the existence of a stable attractor. By becoming close to the sub-harmonic resonance, the energy of the system increases step by step and its responses tend to more complex behavior. By changing the excitation frequency in the range of $\frac{\omega_m}{\omega_n} = [2.49\ 2.55]$, a 2T-periodic behavior might be observed. The more reducing the input speed of the pinion, the more observing high level of instability response. By going downward in terms of excitation frequency, the behavior of the system becomes more complex and aperiodic. To recognize the type of response, further tools such as the largest Lyapunov exponent, fractal dimension, spectra, Poincaré map, phase portrait are required. Chaotic behavior might occur at two separated ranges, it is identified by two different colors of red and pink in Fig. 18. To be more accurate, at $\frac{\omega_m}{\omega_n} = [1.90\ 2.03]$ and $\frac{\omega_m}{\omega_n} = [2.20\ 2.49]$ the system experiences an aperiodic behavior where a strange attractor might exist. In the middle of these ranges, there is a zone where the response of the system is *n*T-periodic; based on the amplitude-frequency diagram, see Fig. 17-a, the system shows a hardening behavior due to backside contact. It started from n = 12 and then tends into n = 4 in a non-smooth path (i.e., jumps into 4T-Periodic response). By moving backward, the response of the system changes from n = 4, and then n = 8, and finally n = 16.

Fig. 18-b represents the forward simulation where the excitation frequency starts from $\frac{\omega_m}{\omega_n} = 1.8$ and it is increased step by step. With respect to the backward simulation, the system exhibits mainly a chaotic behavior. Then by increasing enough the excitation frequency and going far away from the parametric resonance, the response of the system tends to a periodic behavior.

4.4. Chaotic crisis

In this section we investigate the most iconic features that come from observing the bifurcation diagram in Fig. 19, i.e., periodic windows. This periodic window begins with a saddle node bifurcation and ends with an interior crisis [37]. The **chaotic crisis** is a class of global bifurcation. It occurs when a chaotic attractor collides with an unstable periodic orbit or its basin of attraction [38,39]. We can distinguish three types of crises [40].

1) **Boundary crisis**: A system undergoes a boundary crisis when its attractor collides with the basin of attraction separating it from another coexisting attractor. After the crisis, the attractor is destroyed and converted into a nonattracting chaotic saddle. The trajectory then wanders in the vicinity of the saddle for some time before asymptotically approaching the other attractor, producing transient chaos [41,42]. A boundary crisis results in the destruction of a chaotic attractor and occurs due to a tangency between a stable and unstable manifold. This phenomenon happens when the chaotic attractor becomes equal to the closure of the unstable manifold [43, 44].
2) **Interior crisis**: In an interior crisis, a chaotic attractor collides with an unstable periodic orbit or limit cycle within its basin of attraction. When this collision occurs, the attractor suddenly expands in size but remains bounded [45]. An interior crisis occurs when an n-piece chaotic attractor (where n = ¼ 2, 3, …) becomes tangent to its basin of attraction. This happens when the attractor is equal to the closure of the unstable manifold. This can only occur when the stable manifold is not the boundary of the basin of attraction, resulting in an increase in the size of the chaotic attractor [37,43].
3) **Attractor merging crisis** occurs when two or more attractors simultaneously touch a periodic orbit on the basin boundary that separates them.

Boundary and interior crises are also referred to as discontinuous bifurcations, characterized by abrupt changes in the phase space locus of

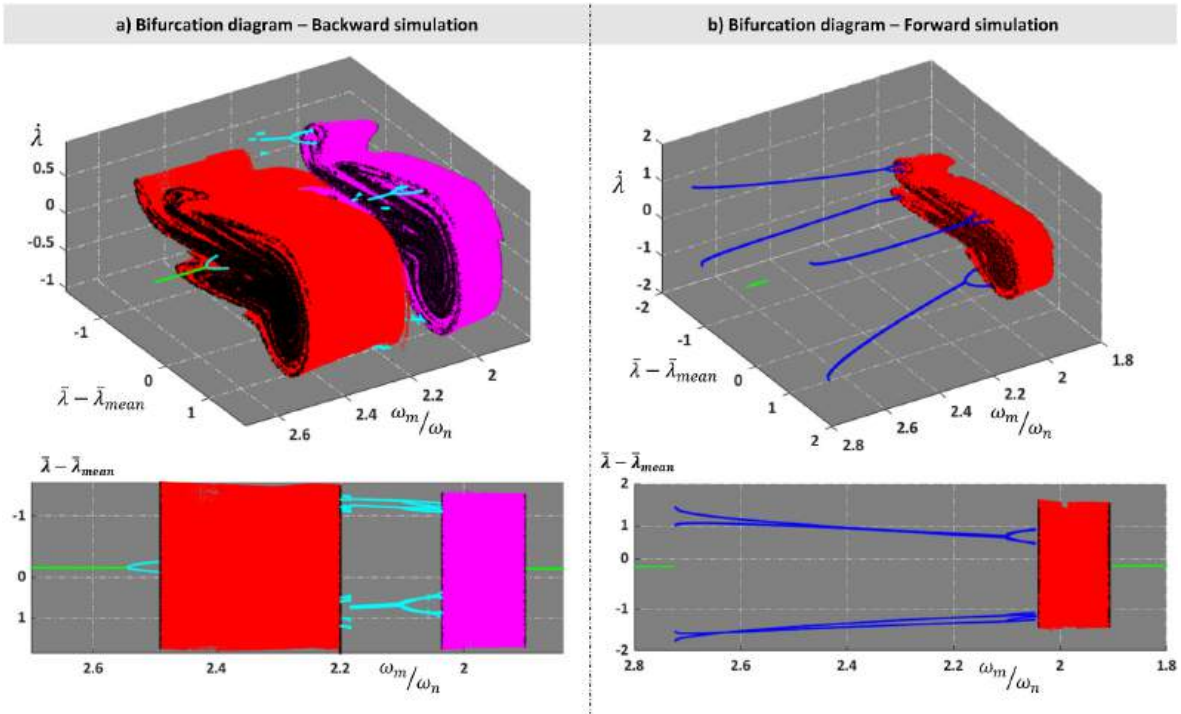

Fig. 18. 3D bifurcation analyses; a) backward simulation, b) forward simulation:
Periodic response; , aperiodic responses, , nT-periodic responses, starting and ending point of chaotic behavior.

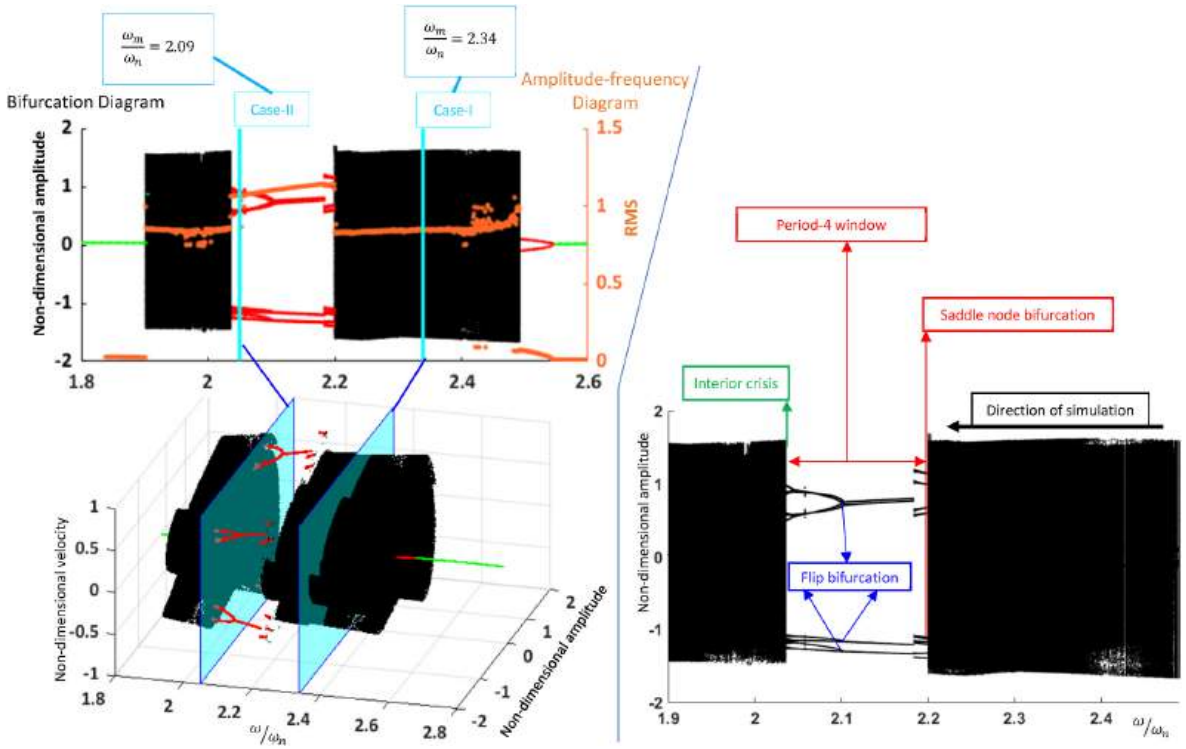

Fig. 19. Nonlinear vibration behavior in different excitation frequency ratios for backward simulation for the system with adaptive MS approach at low-level torque.

an attractor [46–48].

To comprehend the behavior of the system, the extracted results obtained from backward simulation is selected, see Fig. 19. Two cases at two different excitation frequencies, i.e., $\frac{\omega_m}{\omega_n} = 2.09$ and 2.34, are considered to analyze the dynamics of the SBG where the system represents a complexity in terms of nonlinear vibrations. To conduct the analysis, four different tools are employed, i.e., Poincaré map, time history, FFT spectrum, and phase portrait. For each case the developing the trajectory is recorded over passing the time as an animation, see **Supplementary data**.

4.4.1. *Chaotic attractor: Case-I with* $\frac{\omega_m}{\omega_n} = 2.34$

Strange attractors have a number of characteristics: a) they are aperiodic, i.e., they never repeat; b) they exhibit sensitive dependence on initial conditions and hence they are unpredictable in the long term; c) they are governed by one or more control parameters; d) a small change in which can cause the chaos to appear or disappear; and e) their governing equations are nonlinear. More often than not, the orbit or trajectory of a chaotic system will be drawn to a small region of state space as time evolves, whereupon it moves in a deterministic but unpredictable manner on a fractal object called a strange attractor, which are the usual geometric manifestation of chaos. They were originally called '*strange*' because of their fractal structure. The terms '*strange attractor*' and '*chaotic attractor*' are often used interchangeably, according to whether the interest is in their geometrical or dynamical properties, although some authors make a distinction between them [40].

The behavior of the stranger attractor at excitation frequency $\frac{\omega_m}{\omega_n} = 2.34$, is summarized in Fig. 20. Poincaré maps are represented in two different dimensions: 3D and 2D, as shown in Fig. 20-a and Fig. 20-b respectively. The structure of a flow can often be revealed in a Poincaré section [40]. This method reduces the dimension of the attractor by one. The dimensions of the Poincaré section are usually independent of the section taken, as long as it includes the attractor. The reason is that there is a simple mapping from one section to another that preserves the topology, albeit with stretching and distortion. There are infinitely many such sections, and some are more revealing than others. The produced map, i.e., Poincaré map, has a subset of the same dynamics as the corresponding flow.

The tooth separation phenomenon is defined on the Poincaré map with yellow color, for the interval $-1 < \bar{\lambda} < 1$. During the tooth separation, the acceleration, i.e., $\ddot{\bar{\lambda}}$, became constant but not zero due to the oil viscosity in the middle of two mated teeth. This point is clear from Fig. 20-c and d as well, where the phase portrait is represented.

By using the time history shown in Fig. 20-e and calculating the spectrum, it is clear the cloudy zone shown in bifurcation diagram in Fig. 19 causes an strong irregularity in time history response of the system. These aperiodic behaviors in the dynamic response on the system lead to the spreading out of the energy of system over a wide range of frequency, such spreading appear like noise.

4.4.2. *Largest lyapunov exponent and correlation dimension*

To analyze complex nonlinear dynamical systems, computational techniques such as nonlinear time series analysis are used. Chaos arises when infinitesimal disturbances are exponentially amplified, combined with global folding mechanisms that keep solutions within certain bounds. This exponential sensitivity is measured through the spectrum of Lyapunov exponents [49]. In the context of chaos theory, attractors—geometric figures formed by system trajectories—are characterized by fractal dimensions. For attractors originating from regular deterministic systems, such as limit cycles or tori, their fractal dimension matches their topological dimension [25]. Before calculating the largest Lyapunov exponent (LLE), and the correlation dimension, it is necessary to reconstruct the phase space. A widely used technique for phase space reconstruction from a time series is the Method of Delays, which involves determining both the embedding dimension and the delay time. This approach is common in the study of observed time series from nonlinear systems to uncover the underlying dynamics [50]. The delay time is typically selected as the first local minimum of the mutual information function (see Fig. 21-a), while the embedding dimension is determined by applying a 10 % threshold [51] to the fraction of false

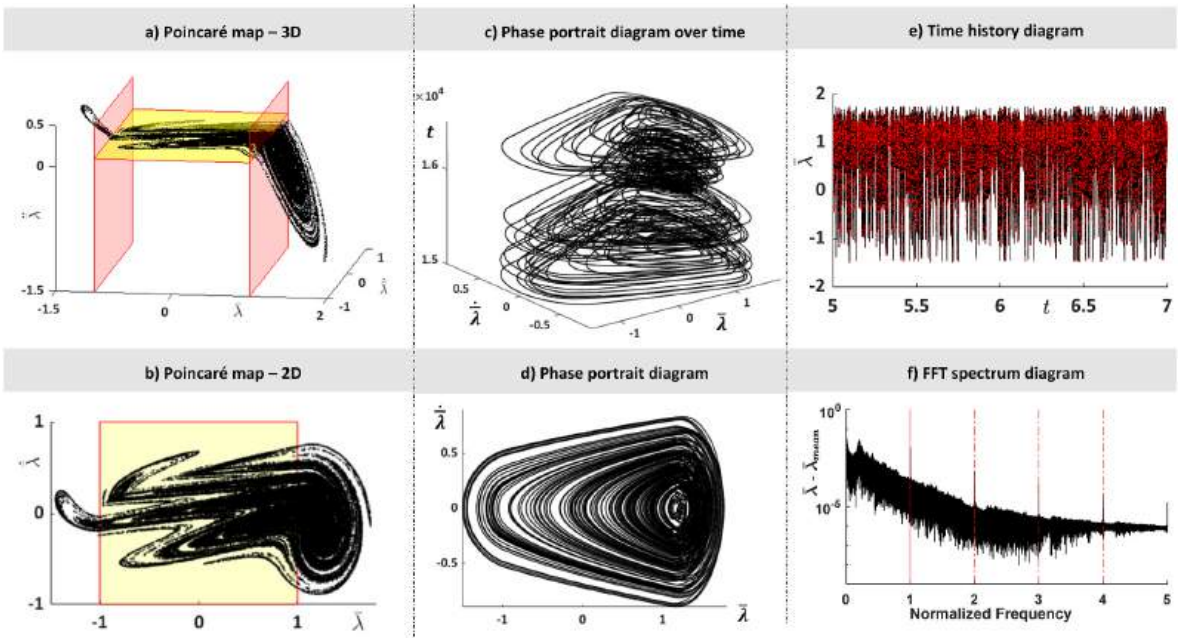

Fig. 20. Dynamic analyses for the case I with $\frac{\omega_m}{\omega_n} = 2.34$

neighbors (see Fig. 21-b).

Based on the previous explanation, we estimate the attractor dimension, i.e., the correlation dimensions of the attractors, and largest Lyapunov exponent. these two parameters are estimated by means of two different approaches: a code written in MATLAB [15], and also the "nonlinear time series analysis package (TISEAN-V3.0.1)" [52]. The number of samples to carry out the time series analysis is 1762112, and the sampling interval for this case is 16. From Fig. 21-a and Fig. 21-b, the λ_{max} *for both approaches is illustrated.*

Fig. 22-c allows for the estimation of the correlation dimension. Considering a neighborhood radius between 9.1×10^{-4} and 13×10^{-2}, the slope of the correlation integral function, multiplied by the sampling interval, provides the correlation dimension. In Fig. 22-d, the slope of the correlation integral is plotted for six different embedding dimensions (m = 5 to 10), with data extracted using the TISEAN package. The results from Fig. 22 are summarized in Table 1. The estimated correlation dimension is found to be 2.8, while the calculated LLE for both methods is positive, indicating a strong aperiodic response in the system. Comparing the results obtained from the TISEAN package and MATLAB code shows less than a 1 % difference in the calculated correlation dimension, with both approaches estimating a positive LLE. This suggests that the system exhibits significant irregularity in its time-histories, with a non-integer correlation dimension of approximately 2.8, highlighting the fractal nature of the attractor that we can claim it is hyper chaos.

4.4.3. *Periodic windows*

Referring to Fig. 19, amongst all the chaos, a stable period-*n* orbit appears at $\frac{\omega_m}{\omega_n} = [2.03\ 2.2]$ where the system is not chaotic. Indeed, there are four miniature bifurcation diagrams with type of route to chaos. As the excitation frequency decreases, the 2T-periodic solution loses its stability, then a period-doubling bifurcation occurs at $\frac{\omega_m}{\omega_n} = 2.55$. As the speed further decreases, the period-doubling bifurcations lead the system to chaos. After that, chaos disappears, and period-halving bifurcations occur. In terms of routes to chaos: It is likely that some routes by which a stable equilibrium becomes chaotic are yet to be identified. Those that result from local (rather than global) bifurcations can be categorized into three basic types: period-doubling, quasiperiodic, and intermittent. Period doubling has been described in connection with the logistic map, but more generally occurs in maps and flows where stable points become unstable in a series of flip bifurcations and subharmonic generation.

The periodic window is a period-4 one which begins with a saddle node bifurcation at $\frac{\omega_m}{\omega_n} = 2.20$, where the structure of the chaotic attractor destroyed into a period-12 orbit. The reason is that to the right of the window is a that gives birth to both a stable and unstable orbit. The stable orbit is evident in the diagram, but the unstable one remains nearby and eventually collides with the attractor as it expands. This orbit then repels the iterates to regions that were not previously accessible. The period-12 stable periodic orbit undergoes a period-tertile bifurcations as the speed decreases and turns eventually into period-4

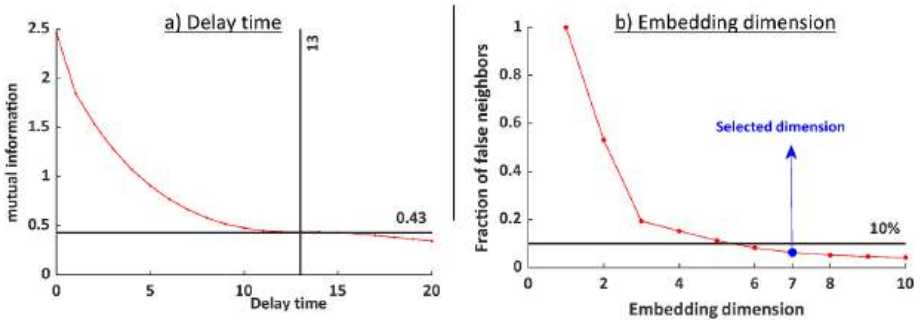

Fig. 21. Extracting a) delay time and b) embedding dimension for the case in backward simulation at $\frac{\omega_m}{\omega_n} = 2.34$

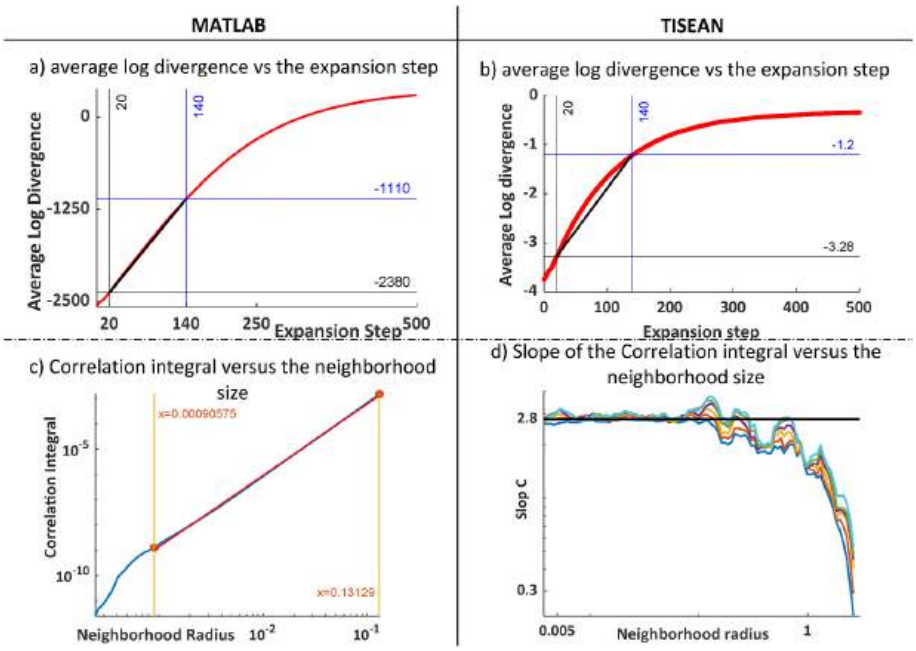

Fig. 22. Extracted largest Lyapunov exponent and correlation dimension from simulation done by TISEAN and MATLAB.

Table 1
Extracted data from nonlinear time series analysis for the case I at $\frac{\omega_m}{\omega_n} = 2.34$

Case study	Correlation dimension	Largest Lyapunov exponent	Delay time	Embedding dimension	Total samples	Sampling interval
MATLAB	2.82	+10.58	13	7	1,762,112	16
TISEAN	2.8	+0.0173				

attractor. And then the periodic attractor born in a period-8 attractor. This period-8 attractor period-doubles to a period-16 attractor, which jumps to a chaotic attractor at $\frac{\omega_m}{\omega_n} \approx 2.03$. Indeed, the period-8 and period-16 orbits are born at $\frac{\omega_m}{\omega_n} \approx 2.1$, and 2.05 respectively.

The Feigenbaum number arises as an eigenvalue of an operator, and hence it is sometimes whimsically called a 'Feigen value', i.e., 'fig tree' in German [53–55]. Some authors, e.g., Strogatz [56], call such a plot an 'orbit diagram'. A remarkable property of the constant Feigenbaum number is its universality, having the same value for all unimodal maps with a quadratic maximum. After initial transients have died away the **Feigenbaum constant** converges to 4.66920 [57], note also that there is no practical use for such precision. In Fig. 23, we highlighted the backward simulation at which the first bifurcation occurred at $\frac{\omega_m}{\omega_n} =$ 2.1025, the second one at $\frac{\omega_m}{\omega_n} = 2.0475$, and third at $\frac{\omega_m}{\omega_n} = 2.036$, then after calculation, the Feigenbaum constant is estimated to be 4.74.

4.4.4. *Period-doubling cascade: Case-II with* $\frac{\omega_m}{\omega_n} = 2.09$

Period doubling can be analyzed across three distinct levels of complexity. The first level involves an individual period-doubling bifurcation. At the second level, we observe an infinite sequence of period doublings, which are interconnected by periodic orbits, forming a structure known as a cascade. This phenomenon, initially described by Myrberg [58] and later elaborated upon by Feigenbaum [54], illustrates the intricate patterns within dynamical systems. The third level deals with an infinite number of cascades and a specific parameter value, μ (controlling parameter), which marks the onset of chaos. At this

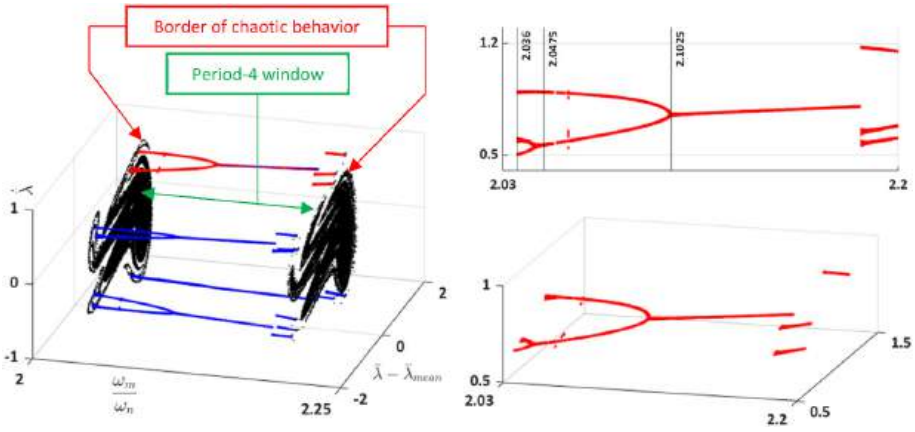

Fig. 23. Representing the periodic window.

parameter value, almost all "regular" periodic orbits (except for a finite number) are connected to a single cascade via regular periodic orbits. Additionally, most cascades are either paired, meaning they are linked to exactly one other cascade, or solitary, meaning they are associated with only one regular periodic orbit at μ. These solitary cascades are notably robust to substantial perturbations [59].

In the range of $\frac{\omega_m}{\omega_n} = [2.03\ 2.2]$ in Fig. 23, where we have a period-doubling cascade resulting in chaos, Let's investigate the dynamic behavior of a case in this range, i.e., case-II with $\frac{\omega_m}{\omega_n} = 2.09$, where the system experienced a 8T-periodic behavior, see Fig. 24. There are some moments that tooth separation occurred in the system, shown with blue box in Fig. 24-d. Poincaré map presents 8 dots which represented an 8T-Periodic dynamic responses; this point is clear from the FFT spectrum diagram where we have at one unite normalized frequency.

4.5. Dynamic mesh torque and spectral analyses

The repetitive dynamic load provides a condition to arise fatigue failure in the tooth root, pitting and scoring on the teeth surface. Therefore, dynamic mesh force is a key parameter when it comes to gear manufacturing. Due to variation of pitch radius of the SBG-tooth from heel to toe, we introduce the concept of dynamic mesh torque (DMT) directly related to the dynamic mesh force. The DMT is evaluated by the following definition [7,27].

$$DMT_{pinion} = r_p[C_m(\dot{\lambda} - \dot{e}) + K_m f(\lambda - e)] \tag{19}$$

Fig. 25-a represents the DMT for the case at nondimensional excitation frequency $\frac{\omega_m}{\omega_n} = 2.09$. This frequency is close to the parametric resonance region. In some segments of period, DMT values vanish, i.e., loss of contact, and in some segments of period, DMT values are reversed due to backside contact. This behavior is completely expected from amplitude-frequency diagram where rightward-leaning resonant response indicated hardening nonlinearity due to combination of backside contact and tooth separation phenomena.

Another insightful investigation is the analysis of the spectrum which reveals a series of peaks at discrete frequencies, signifying the presence of a periodic behavior with minor fluctuations over time. The strength of this periodic behavior is crucial; pronounced and distinct peaks multiple of the meshing frequency denote a robust periodicity within the system. Conversely, if the periodic behavior is weaker and less prominent, the spectrum will lack distinct peaks, resembling a continuous band with some degree of variability or sidebands in the case of quasi-periodicity. This suggests a more intricate dynamic. Notably, during spectrum examination, constant frequency shifts, denoted as β_2, may be observed, representing beat frequencies of a quasi-periodic motion. Consequently, th approximate period of the torus cycle can be estimated as: $T_{\text{torus}} \approx 2\pi/\beta_2$. The distribution of the remaining incommensurate frequency peaks in the spectrum is governed by the following formula [24]:

$$\Omega_n = \Omega_0 + n\cdot\beta_2 \tag{20}$$

Where Ω_n *is known also as the second disproportionate frequency, and* n is the number of tori frequency; nD-torus or n-frequency quasiperiodic solution. Besides, the third disproportionate frequency can be described as:

$$\Omega_{n,m} = \Omega_n + m\cdot\beta_1 \tag{21}$$

Where, n and m are the number of frequency peaks. By considering spectrum, Fig. 25-b, and time history diagram, Fig. 25-c, for the case II, $\frac{\omega_m}{\omega_n} = 2.09$, we can calculate the T_{torus} and constant frequency shifts as follows:

$$\begin{aligned}
\bar{\beta}_1 &= 0.25 \times (2.09 \times 17957) = 9382.5\frac{\text{rad}}{s}\\
\bar{\beta}_2 &= 0.125 \times (2.09 \times 17957) = 4691.2\frac{\text{rad}}{s}\\
T_1 &\approx \frac{2\pi}{\beta_1} = \frac{2\pi}{9382.5} = 0.00067s\\
T_2 &\approx \frac{2\pi}{\beta_2} = \frac{2\pi}{4691.2} = 0.00134\ s
\end{aligned} \tag{22}$$

4.6. Recurrence plot and its quantification

Henri Poincaré (1890) [60] and William Feller (1950) [61] introduced the formal concept of recurrences in their groundbreaking work. Indeed, Poincaré's recurrence theorem states that a conservative system will eventually return to a state arbitrarily close to its initial condition. Fascinatingly, this theory echoes Friedrich Nietzsche's philosophical concept of eternal recurrence, where he suggests that all events in life

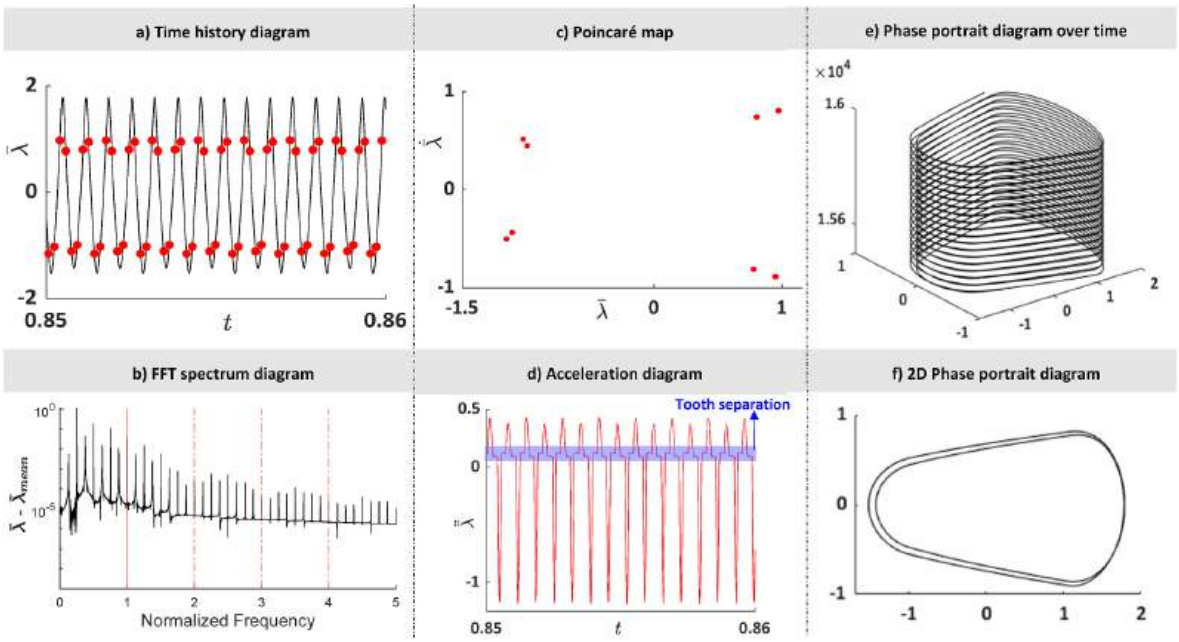

Fig. 24. Dynamic analyses for the case II with $\frac{\omega_m}{\omega_n} = 2.09$

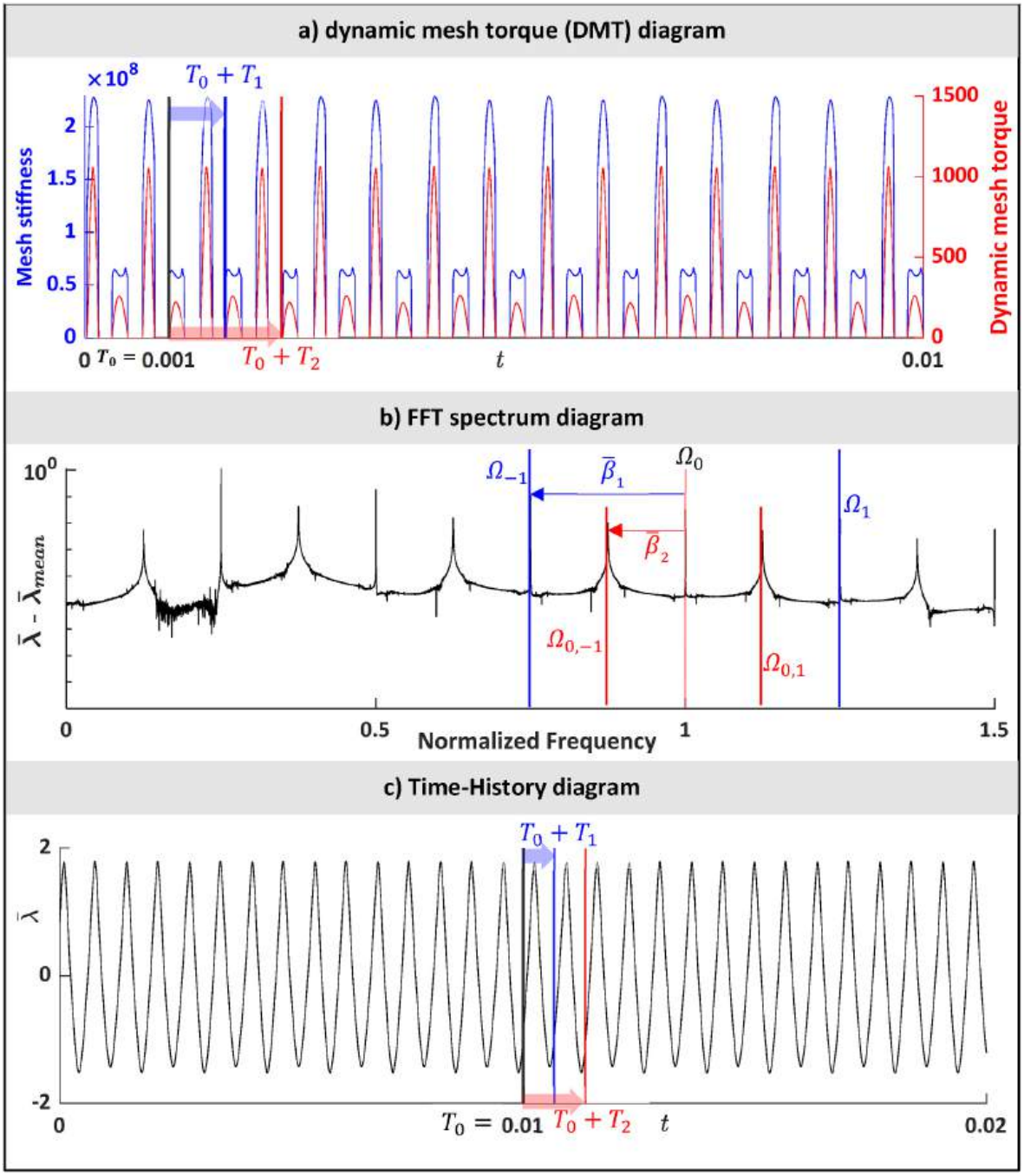

Fig. 25. Periodic analyses for the case II with $\frac{\omega_m}{\omega_n} = 2.09$

perpetually repeat in an infinite cycle. Later, in 1987, Eckmann et al. [20] introduced recurrence plots (RPs) to visually represent the recurrences in dynamical systems. RPs relies on analyzing phase space trajectories. Recurrence, a fundamental attribute of dynamical systems, can be utilized to describe the system's behavior within phase space [62, 63].

Recurrences can be detected in all systems, but the patterns in the plots vary significantly. Periodic motion appears as long, uninterrupted diagonal lines, with the vertical distance between these lines indicating the oscillation period. Conversely, the RP of an uncorrelated stochastic signal consists of numerous isolated black points, resulting in a rather erratic distribution. Originally, RPs were designed to visualize trajectories in phase space. They provide valuable insights into the time evolution of these trajectories, as specific patterns in RPs correspond to distinct system behaviors. For instance, periodic and quasi-periodic systems exhibit RPs with diagonal, periodic, or quasi-periodic recurrent structures, such as diagonal lines or checkerboard patterns. A diagonal line signifies that a segment of the trajectory runs nearly parallel to another segment. Vertical (or horizontal) lines indicate a time interval where the state remains constant or changes very slowly. Bowed lines, with non-constant slopes, reflect the local time relationship between the corresponding close trajectory segments [63,64].

4.6.1. *Required parameters*

The states of natural or technical systems typically change over time, often in complex ways. A dynamical system is characterized by a phase space, continuous or discrete time, and a time-evolution law [63]. Recurrences occur within the phase space of these systems. To analyze

univariate time series using RPs, we reconstruct the phase space through delay embedding. For effective time series analysis, the embedding parameters—dimension m and delay τ—must be chosen correctly. Several methods have been proposed for estimating the smallest sufficient embedding dimension, such as the false nearest-neighbors algorithm [16,65], as well as determining an appropriate delay time τ, using techniques like the auto-correlation function and the mutual information function (see Refs. [16,65,66]).

Embedding: When only a scalar time series is available, the phase space needs to be reconstructed using techniques such as delay embedding. However, this process can introduce numerous spurious correlations in the system under consideration, which manifest in the RPs. In cases of high embedding, even uncorrelated time series may exhibit distinct diagonally oriented structures in the RPs. Although diagonal structures are expected to be uncommon for uncorrelated data, an increase in embedding dimension can eliminate single recurrence points (representing uncorrelated states) and highlight diagonal structures as diagonal lines (representing correlated states). Consequently, any quantification of RPs based on diagonal lines is affected. Therefore, caution must be exercised when interpreting and quantifying structures in RPs of measured systems. Inappropriately high embedding dimensions can lead to the appearance of spurious long diagonal lines in the RP. To mitigate this issue, embedding parameters should be carefully chosen, or alternative quantification measures independent of embedding dimensions should be employed. The presence of spurious correlations in RPs due to embedding can also be rationalized by noting that an RP computed with any embedding dimension can be derived from an RP computed without embedding ($m = 1$) [63,67,68].

Threshold ε: The threshold ε is a crucial parameter in generating recurrence plots (RPs), thus necessitating careful consideration in its selection. If ε is chosen too small, the resulting plot may contain few recurrence points, providing limited insight into the underlying recurrence structure of the system. Conversely, selecting ε too large results in nearly every point being a neighbor of every other point, leading to numerous artifacts. A large ε can also incorporate points into the neighborhood that are merely consecutive points on the trajectory, a phenomenon known as tangential motion. This can inflate diagonal structures in the RP, misrepresenting their actual characteristics. Therefore, a balance must be struck in determining the value of ε. Additionally, the presence of noise may necessitate selecting a larger threshold to preserve any existing structure in the RP. Various "rules of thumb" for choosing ε have been proposed, such as setting it to a few percent of the maximum phase space diameter [69] or ensuring it does not exceed 10 % of the mean or maximum phase space diameter [70,71]. Another approach involves scaling ε according to the recurrence point density of the RP, although this may not be suitable for non-stationary data. In such cases, it has been suggested to set ε such that the recurrence point density is approximately 1 % [72]. For (quasi-)periodic processes, optimal thresholds can be determined by analyzing the density distribution of recurrence points along diagonals parallel to the Line of Identity (LOI), the main diagonal line of the RP [73].

4.6.2. Structures in RPs

As already mentioned, the primary objective of RPs is to visualize trajectories in phase space, a particularly advantageous approach for high-dimensional systems. RPs offer valuable insights into the time evolution of these trajectories, as typical patterns within RPs are indicative of specific system behaviors. These large-scale patterns in RPs can be categorized as follows [20,64].

- **Homogeneous RPs**: Characteristic of stationary systems with short relaxation times compared to the time spanned by the RP. An example is the RP of a stationary random time series (Fig. 26-A).
- **Periodic and Quasi-periodic RPs**: Typically observed in periodic or quasi-periodic systems, featuring diagonal-oriented recurrent structures such as diagonal lines or checkerboard patterns. Fig. 26-B illustrates the RP of a periodic system with two harmonic frequencies, showing a frequency ratio of four with distinct recurrent structures. Irrational frequency ratios result in more complex quasi-periodic structures where the distances between diagonal lines vary. Even for systems with less discernible oscillations, RPs remain useful.
- **Drift**: Evident in systems with slowly varying parameters, indicating non-stationary behavior. The RP gradually fades away from the LOI (Fig. 26-C).
- **Abrupt Changes and Extreme Events**: Manifested as white areas or bands in the RP (Fig. 26-D). RPs facilitate the identification and assessment of extreme and rare events by analyzing the frequency of their recurrences.

Further examination of RPs unveils intricate small-scale structures known as texture [20]. These textures can typically be classified into several categories, including single dots, diagonal lines, and vertical and horizontal lines. The combination of vertical and horizontal lines forms rectangular clusters of recurrence points. Additionally, bowed lines may also appear [20,64].

- **Single**, isolated recurrence points may appear when states are rare, persist for a very short time, or exhibit strong fluctuations.
- **Diagonal lines** occur when trajectory segments run almost parallel to each other. The length of these diagonal lines corresponds to the duration of similar local trajectory evolution. These structures are typically parallel to the Line of Identity, although diagonal structures perpendicular to the LOI may also arise, indicating mirrored trajectory segments and potentially suggesting inappropriate embedding.
- **Vertical (horizontal) lines** denote time intervals during which the state remains unchanged or changes very slowly, indicating a laminar state or intermittency [74].
- **Bowed lines** have a non-constant slope, their shape depending on the local time relationship between corresponding trajectory segments.

Diagonal and vertical lines serve as the foundation for quantitative RP analysis. In general, line structures in RPs locally depict the time relationship between close trajectory segments [75]. To summarize the explanations regarding typology and texture, a list of features and their corresponding interpretations is presented in Table 2.

The visual interpretation of recurrence plots (RPs) requires some expertise. RPs of paradigmatic systems offer valuable insights into characteristic typology and texture (see Fig. 26), serving as instructive examples. However, for a more objective investigation of the system under consideration, quantification of the obtained structures is necessary. These considerations are particularly relevant for systems with characteristic frequencies significantly lower than the sampling frequency of observation. If the sampling frequency is only one magnitude higher than the system's frequencies, and their ratio is not an integer, some recurrences may go undetected [76]. This discretization effect results in noticeable gaps in the recurrence plot, the extent of which depends on the modulation of the system's frequencies (see Fig. 27).

It should be emphasized again that the recurrence of states is a fundamental concept in the analysis of dynamical systems. In addition to recurrence plots (RPs), various other methods based on recurrences exist, such as recurrence time statistics [77,78] first return map [79], space time separation plot [80] and recurrence-based measures for detecting non-stationarity (which are closely related to recurrence time statistics) [81].

4.6.3. Recurrence quantification analysis (RQA)

Recurrence Plots offer valuable insights into the dynamics of dynamical systems. However, when displayed graphically with inadequate resolution, RPs can pose challenges, as users must subjectively interpret the patterns and structures within them. Moreover, different observers may perceive these patterns differently. To address this

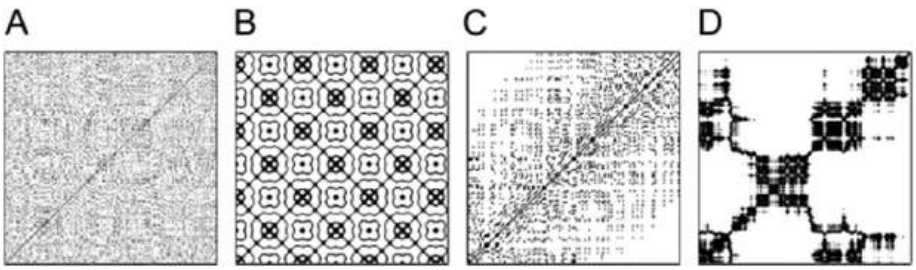

Fig. 26. Characteristic typology of recurrence plots: A) homogeneous: represented by uniformly distributed white noise, B) periodic: demonstrated by superimposed harmonic oscillations, C) drift: evident in systems corrupted with a linearly increasing term, such as a logistic map, D) disrupted: represented by processes like Brownian motion [63].

Table 2
RPs patterns and their meanings [63].

Homogeneity: Indicates a stationary process.
Fading to the upper left and lower right corners: Suggests non-stationary data with a trend or drift present.
Disruptions (white bands): Signify non-stationary data where some states are rare or deviate significantly from the norm, potentially indicating transitions.
Periodic/quasi-periodic patterns: Reflect cyclicities in the process, with the time distance between periodic patterns corresponding to the period. Varying distances between long diagonal lines indicate quasi-periodic processes.
Single isolated points: Suggest strong fluctuations in the process. If only single isolated points are present, the process may be uncorrelated random or even anti-correlated.
Diagonal lines (parallel to the LOI): Indicate similar state evolution at different epochs, potentially suggesting a deterministic process. If these diagonal lines coexist with single isolated points, chaotic behavior may be indicated. Periodic diagonal lines may suggest unstable periodic orbits.
Diagonal lines (orthogonal to the LOI): Suggest similar state evolution at different times but with reverse time, sometimes indicating insufficient embedding.
Vertical and horizontal lines/clusters: Indicate states that do not change or change slowly for a period, typically representing laminar states.
Long bowed line structures: Suggest similar state evolution at different epochs but with varying velocity, potentially indicating changing dynamics of the system.

subjectivity, in the early 1990s, Zbilut and Webber introduced definitions and procedures to quantify RP structures [71,82,83]. They established a set of five recurrence variables as complexity measures, primarily focusing on diagonal line structures in RPs, and termed the methodology Recurrence Quantification Analysis [15,63,64,84,85].

1. **percent recurrence (REC) or recurrence rate (RR)**; simply enumerates or counts the black dots in the RP while excluding the Line of Identity (LOI). This measure provides insight into the relative density of recurrence points within the sparse matrix.
2. **percent determinism (DET);** Systems with deterministic dynamics are often characterized by diagonal lines in recurrence plots, indicating repeating recurrences within a state. In periodic signals, these diagonal lines tend to be long, while in chaotic signals, they are shorter. In stochastic signals, diagonal lines are generally absent, except for occasional chance recurrences forming very short lines. DET can be interpreted as a measure of the predictability of the system, particularly for periodic behaviors compared to chaotic processes. However, it's important to note that DET does not strictly represent the determinism of a process.
3. **maximal line length in the diagonal direction (L_{max})**; simply refers to the length of the longest diagonal within the entire recurrence plot (RP). Diagonal structures in RPs indicate segments of the trajectory that are close to each other at different times, providing insight into the divergence of trajectory segments. The smaller L_{max} suggests more divergent trajectories. There exists a relationship between L_{max} and the largest positive Lyapunov exponent (if present in the system). This relationship can be elucidated by examining the (cumulative) frequency distribution of diagonal line lengths and the entropy, which serves as a lower limit of the sum of the positive Lyapunov exponents.
4. **Shannon entropy of the frequency distribution of the diagonal line lengths (ENT)**; The entropy (ENT) metric reflects the complexity of the deterministic structure within the system. Expressed in bits per bin, higher ENT values signify greater dynamical complexity. For instance, in the case of uncorrelated noise or simple oscillations, ENT values tend to be relatively small, indicating lower complexity. It is worth noting that ENT is sensitive to the number of bins used and may vary depending on different parameter choices for the same process, such as different thresholds ε.
5. **trend (TND);** This metric represents the linear regression coefficient over the recurrence point density of the diagonals parallel to the Line of Identity (LOI). TND provides insights into the stationarity or non-stationarity of the process. In quasi-stationary dynamics, TND values

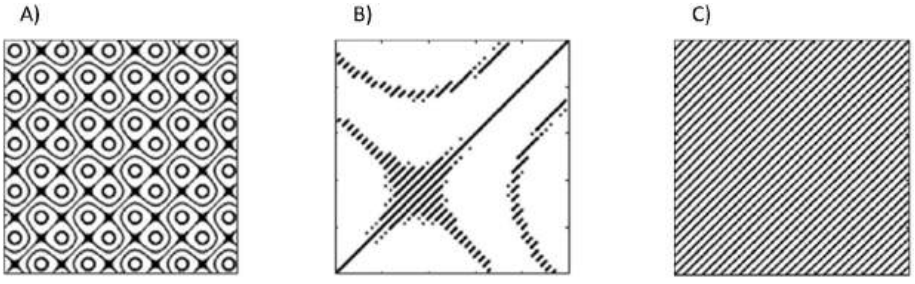

Fig. 27. A) characteristic patterns of gaps (all white areas) in a recurrence plot of a modulated harmonic oscillation, e.g., $\cos(2\pi 1000t) + 0.5\sin(2\pi 25t)$, sampled with a frequency of 1 kHz. B) magnified detail of the RP shown in (A), revealing the actual periodic line structure resulting from the oscillation but disturbed by extended white areas. C) corresponding RP as depicted in (B), but for a higher sampling rate of 10 kHz. The periodic line structure due to the oscillation now covers the entire RP [63].

tend to hover near 0, indicating stability. Nonstationary dynamics will have TND values far from 0 revealing drift in the dynamics possibly indicating that the system is en route between more stationary states.

The five RQA variables outlined above primarily focus on the lengths, number, and distributions of diagonal lines in RPs, which are sensitive to parallel trajectories along different segments of the time series. However, RPs also contain vertical and horizontal elements in addition to diagonal lines. Marwan et al. [74] have proposed additional recurrence quantifications based on these vertical lines.

6. **laminarity (LAM);** shares a similar definition to that of DET. It indicates the percentage of recurrent points found in vertical structures, while DET represents the percentage of recurrent points in diagonal structures.
7. **trapping time (TT);** denotes the average length of vertical structures. TT encapsulates details about the quantity and duration of vertical structures in the RP, indicating the average time the system remains in a specific state (the duration of the state's trapping).
8. **maximal length of the vertical structures (V_{max});** represents the longest vertical line in the RP. While the dynamical interpretation of V_max has not been definitively outlined, it may be associated with singular states where the system remains trapped, forming rectangular patterns in the RP.

Unlike the five fundamental RQA measures, these new measures have the capability to detect chaos-chaos transitions [74]. Consequently, they enable the exploration of intermittency, even in cases where it manifests in short and nonstationary time series.

4.6.4. Nonlinear dynamic analyses based on recurrence plot

As explained, the recurrence analysis serves as an effective tool for characterizing and quantifying the dynamics of complex systems, such as laminar, divergent, or nonlinear transition behaviors [86]. Now Let use the concept of recurrence for the analysis of data and to study the dynamics of the SBG systems.

In this study, two CRP MATLAB toolboxes are used to plot the RPs. The algorithms of the toolboxes have been programmed by Marwan [63, 87], Method #1, and Yang [86,88], Method #2. To ensure extracted results are accurate enough, these two approaches are chosen in order to compare their results. First simulation is carried out on a periodic case whose RPs pattern is known, i.e., diagonal lines. The excitation frequency of the case is $\frac{\omega_m}{\omega_n} = 2.60$ with 241 samples per each period which is clear from Fig. 28-f where the distance between two lines is 241. Fig. 28 represents all dynamical results and as it is excepted, we observe diagonal lines in recurrence plot. All lines are not exactly at the same thickness and the reason is due to some very weak irregularity which can be observed on phase diagram and Poincaré map.

It is interesting to visualize the dynamics of the SBG-system by recurrence plot for two cases where we observed 8T-periodic and aperiodic behavior at $\frac{\omega_m}{\omega_n} = 2.09$, and 2.34 respectively, see Fig. 29. RPs is based on the computation of a distance matrix between rows of embedded points in the time series of interest [84]. For the present analysis:

- **case I**: an embedding dimension of 7 was selected with a lag of 13 for 26800 consecutive points; considered last 100 periods.
- **case II**: an embedding dimension of 6 was selected with a lag of 10 for 30000 consecutive points; considered last 100 periods.

From Table 3, we can conclude that:

Recurrence Rate (RR); $RR_{8T-Periodic} > RR_{Chaos}$: in Periodic System, the recurrence rate would be high, indicating frequent returns to previously visited states due to the regular, repeating nature of the motion. In chaotic System, the recurrence rate would be lower compared to the periodic system, reflecting the less frequent and more irregular returns to prior states.

Determinism (DET); $DET_{8T-Periodic} \geq DET_{Chaos}$: in periodic System, DET is higher as the system exhibits predictable, i.e., regular patterns. The RP will show long, uninterrupted diagonal lines. While, in Chaotic System, DET is lower as the system's behavior is less predictable and more complex. The RP will show shorter, fragmented diagonal lines.

Longest Diagonal Line (L_{max}); $L_{max8T-Periodic} > L_{maxChaos}$: in periodic System, the longest diagonal line would be quite long, reflecting the

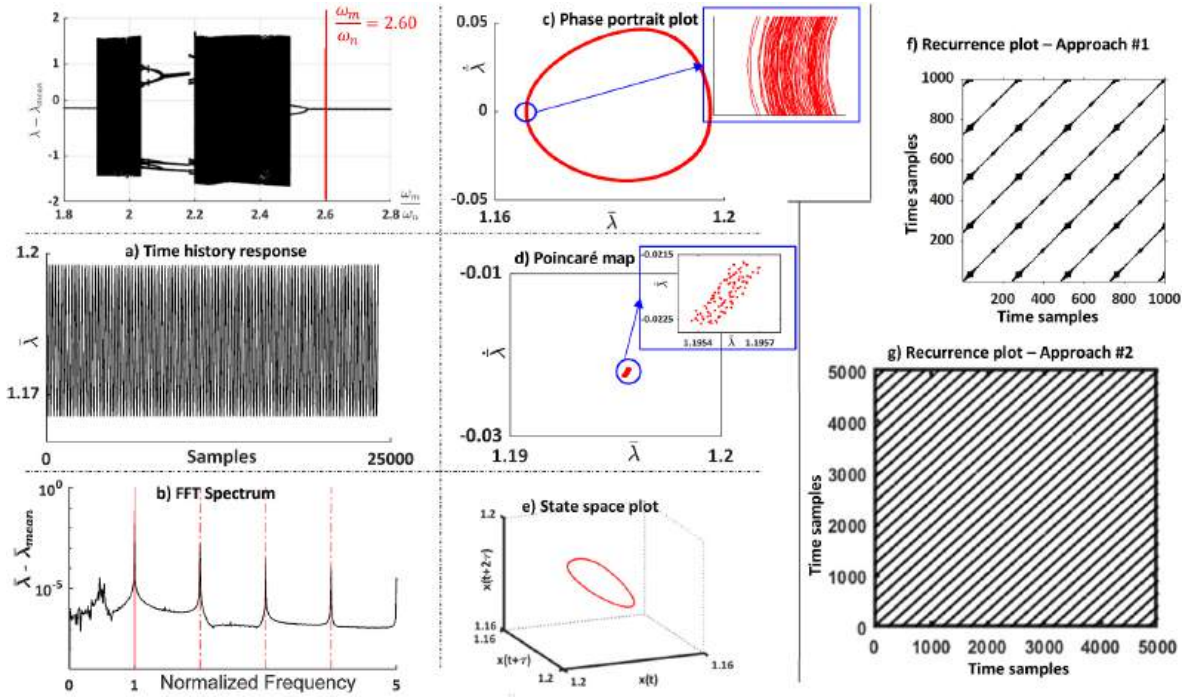

Fig. 28. Dynamic response of the periodic case at $\frac{\omega_m}{\omega_n} = 2.60$ with embedding dimension of 3, lag of 7, and threshold of 0.001.

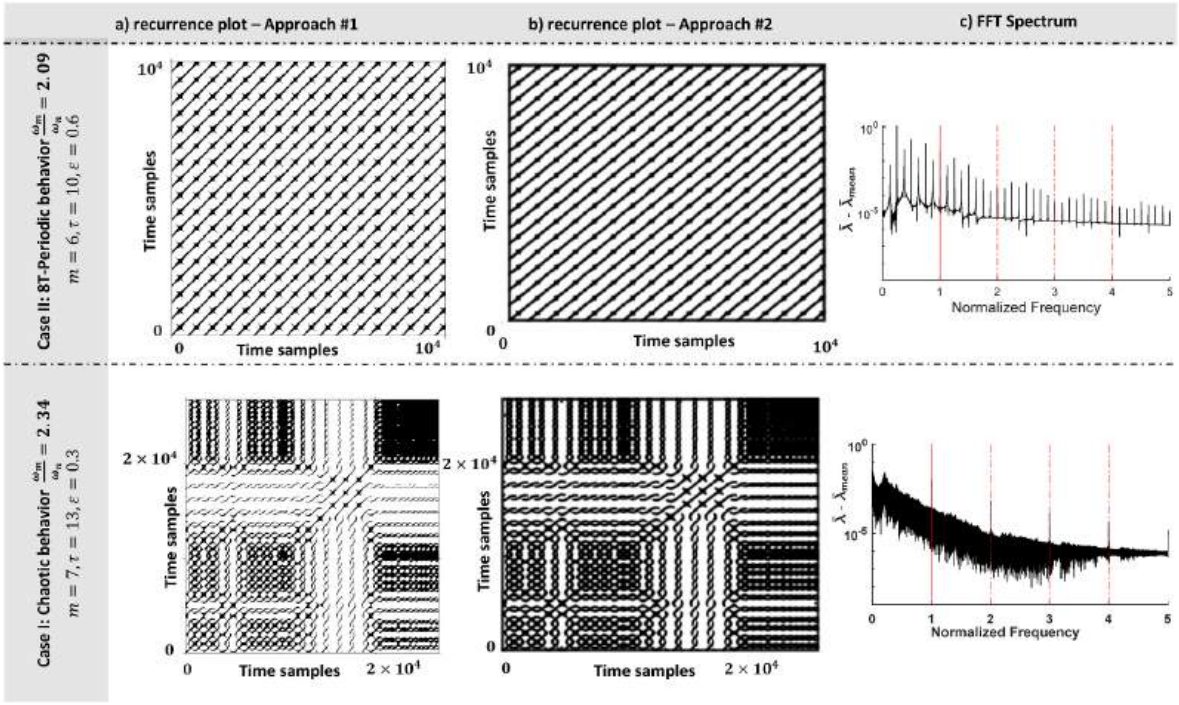

Fig. 29. Recurrence plots for two defined cases at excitation frequencies of 2.09 and 2.34.

extended periods of regular, i.e., repeating patterns. However, in chaotic System, the longest diagonal line would be shorter, due to the inherent instability and unpredictability of the chaotic system.

Entropy (ENT); $\mathbf{ENT}_{8T-Periodic} < \mathbf{ENT}_{Chaos}$: in periodic System, the entropy is lower, as the diagonal line lengths are more uniform, and the system is highly predictable. In chaotic System, entropy is higher, indicating a greater diversity of diagonal line lengths and higher complexity in the system's behavior.

Trapping Time (TT); $\mathbf{TT}_{8T-Periodic} < \mathbf{TT}_{Chaos}$: in Periodic System, trapping times is short, as the system does not linger in a single state for long. While, in chaotic System, trapping times are longer, indicating that the system can remain in certain states for extended periods.

5. Conclusion

In this study, a comprehensive analysis was conducted to evaluate the effect of considering the nonlinearity emanating from the Hertzian contact stress on the dynamic response of the SBG system. To do that, two approaches are considered to solve the governing equation of motion: conventional approach which is average-MS method and the proposed approach which is adaptive-MS. The considered spiral bevel gear pair is a real model used in helicopter transmission systems. The primary goal was to compare two approaches for determining MS – the average slope approach (average-MS) and an adaptive hybrid analytical-computational approach (adaptive-MS) – and to assess their effectiveness in dynamic simulations. The research demonstrated the significant role of nonlinearity in gear dynamics and underscored the necessity of accurate MS calculations for predictive maintenance and system optimization. The findings contribute valuable insights into the behavior of complex gear systems under varying operational conditions. The main key point can be mentioned as follows:

Methodologies Compared: The average-MS approach, which uses an average slope calculation, and the adaptive-MS approach, which integrates Hertzian contact stress nonlinearity and polynomial regression, were both applied to determine MS. The adaptive-MS method proved to be superior in accurately representing the MS variations during dynamic simulations.

Mesh stiffness simulation: More than 830 semi-static simulations were performed using Transmission3D-Calyx, and a MATLAB script automated the process of running simulations, extracting results, and updating the input torque iteratively. Twenty-one-time steps captured the dynamics of tooth contact and separation, highlighting the importance of precise time-dependent MS evaluation. The adaptive-MS approach's results were validated against Nonlinear Finite Element Method (Nonlinear-FEM) simulations, showing excellent agreement. The study found that the biggest difference between the adaptive-MS and FEA methods occurred at specific time steps, with an overall average difference of 1.7 %, underscoring the accuracy of the adaptive-MS approach.

Dynamic Analysis: The governing equation, which is a non-smooth and non-autonomous dynamical model, is solved by GearDyns-SBG program. It constructs amplitude–frequency diagrams and time-history responses of the system by varying the excitation frequency (pinion rotation speed). The program performs simulations using two concepts: backward simulation (from high to low speed) and forward simulation (from low to high speed). This dual simulation ensures that all stable branches, particularly the softening branches, are followed. The dynamic behavior was characterized using nonlinear time series analyses, including Lyapunov exponents, fractal dimension evaluations, 2D and 3D bifurcation diagrams, amplitude-frequency analyses, Poincaré maps, phase diagrams, recurrence plots, and recurrence quantification analyses.

Practical Implications: The adaptive-MS approach enables real-time updates of MS based on varying DMT and time, making it highly applicable for real-time simulations and predictive maintenance. This

Table 3
Calculated features of recurrence quantification analysis.

	RR	DET	L_{max} [points]	ENT [bits/bin]	TT
Case I: Chaotic system	0.1465	0.9998	40121	5.6	102.99
Case II: 8T-periodic system	0.2275	1	44979	4.23	84.84

method can potentially be extended to other gear systems, enhancing the precision and reliability of dynamic simulations across various applications.

CRediT authorship contribution statement

Moslem Molaie: Writing – review & editing, Writing – original draft, Visualization, Validation, Methodology, Investigation, Formal analysis, Data curation, Conceptualization. **Antonio Zippo:** Writing – review & editing, Writing – original draft, Resources, Methodology, Investigation, Funding acquisition, Formal analysis, Conceptualization. **Francesco Pellicano:** Writing – review & editing, Writing – original draft, Supervision, Resources, Project administration, Methodology, Investigation, Funding acquisition, Formal analysis, Conceptualization.

Funding source declaration

The financial support provided by the Funding body – Region Emilia Romagna PR FESR 2021–2027 Action 1.1.2, titled "THEORETIC", C.U.P. E67G22000610001.

Declaration of competing interest

The authors declare that they have no known competing financial interests or personal relationships that could have appeared to influence the work reported in this paper.

Acknowledgments

The authors thank Dr. Giorgo Bonori and Advanced Numerical Solutions, Inc. for providing Transmission3D software and their support.

Appendix A. geometric parameters of the considered SBG.

Table 4
General data

Hand of pinion	Left
Shaft offset	0
Shaft angle	90 deg
Loaded side of gear	Convex
Driver	Pinion
Coefficient of friction	0
Pinion speed [rpm]	100
Diametral pitch [1/in]	5.141
Applied torque on the pinion [N.m]	179.04

Table 5
Pinion and gear data

Tooth parameters			Pinion	Gear
No. of teeth			12	36
Transverse circular tooth thickness at pitch cone [in]			0.32	0.15
Outer cone distance [in]			3.691	3.691
Face width [in]			1.0	1.0
Face angle [deg]			22.31667	72.5
Back angle [deg]			18.433	71.5666
Spiral angle [deg]			35	35
Pitch angle [deg]			18.433	71.5666
Young's modulus [psi]			30.0×10^6	30.0×10^6
Poisson's ratio			0.3	0.3
Machine settings	Concave	Convex	Concave	Convex
Radial setting [in]	2.947802	2.801049	2.85995	2.85995
Blank offset [in]	0.1545759	−0.1742616	0	0
Root angle [deg]	16.8666	16.8666	67.68333	67.68333
Machine center to back [in]	−0.04023062	0.05414291	0	0
Sliding base [in]	0.01167273	−0.01570932	0	0
Cradle angle [deg]	63.94203	53.92599	59.2342023	59.2342023
Ratio of roll	3.242698536	3.105176807	1.051674445	1.051674445
Cutter geometry	Concave	Convex	Concave	Convex
Cutter type	Straight	Straight	Straight	Straight
Point radius [in]	2.965621	3.071306	3.0325	2.9675
Blade angle [deg]	18.6015	24.90	22.0	22.0
Edge radius [in]	0.045	0.045	0.01	0.01

Appendix B. Definition of parameters in the present study.

1. Abbreviation:

Table 6
used abbreviation in the current paper

Abbreviation	Meaning
MS	Mesh stiffness
SBG	Spiral bevel gear
DOF	Single degree of freedom
DMF	Dynamic mesh forces
RPs	Recurrence plots
RQA	Recurrence quantification analysis
LLE	Largest lyapunov exponent
DTE	Dynamic transmission error
DMT	Dynamic mesh torque
LSTE	Loaded static transmission error
GTE	Geometric transmission system
UTCA	Unloaded tooth contact analysis
LTCA	Loaded tooth contact analysis
FEA	Finite element analysis
FEM	Finite element method

2. Main parameters:

Table 7
definition of considered parameters

Applied torque	T	Base radius	r_b
Mesh frequency	ω_m	Number of pinion teeth	N_p
Input shaft speed	n_s	Equivalent meshing stiffness	K_m
Number of harmonics	s	Number of samples for UTCA and LTCA	N_1
Half of the gear backlash	b	Mesh damping	C_m
Mean radius at meshing point of pinion	r_p	*Mean radius at meshing point* of gear	r_g
Geometric transmission error	e	Linear dynamic transmission error	λ
Rotational inertia of pinion	I_p^x	Rotational inertia of gear	I_g^y
Normal pressure angle	α	The spiral angle	β
Backlash function	$f(\lambda - e)$	Mean value of mesh stiffness	k_0
Constant output torque	T_l	Constant input torque	T_m
Damping ratio	ξ		

Appendix C. Constant coefficients of the polynomial function for the forward and backward motions.

Table 8
Constant coefficients of the polynomial function with degree $n = 9$ in terms of the forward motion

Time step	a_1	a_2	a_3	a_4	a_5	a_6	a_7	a_8	a_9	a_{10}
$i = 1$	-4.0×10^{-34}	8.7×10^{-30}	-8.0×10^{-26}	4.0×10^{-22}	-1.2×10^{-18}	2.2×10^{-15}	-2.5×10^{-12}	1.8×10^{-09}	-2.1×10^{-06}	3.2×10^{-04}
$i = 2$	-6.3×10^{-34}	1.3×10^{-29}	-1.2×10^{-25}	5.8×10^{-22}	-1.7×10^{-18}	2.9×10^{-15}	-3.0×10^{-12}	2.0×10^{-09}	-2.2×10^{-06}	3.7×10^{-04}
$i = 3$	-5.8×10^{-34}	1.2×10^{-29}	-1.1×10^{-25}	5.3×10^{-22}	-1.5×10^{-18}	2.7×10^{-15}	-2.8×10^{-12}	2.1×10^{-09}	-2.3×10^{-06}	4.2×10^{-04}
$i = 4$	-4.6×10^{-34}	9.6×10^{-30}	-8.4×10^{-26}	4.0×10^{-22}	-1.1×10^{-18}	2.0×10^{-15}	-2.2×10^{-12}	1.9×10^{-09}	-2.4×10^{-06}	4.7×10^{-04}
$i = 5$	-3.4×10^{-34}	7.0×10^{-30}	-6.1×10^{-26}	2.9×10^{-22}	-8.2×10^{-19}	1.5×10^{-15}	-1.9×10^{-12}	1.9×10^{-09}	-2.6×10^{-06}	5.2×10^{-04}
$i = 6$	-1.3×10^{-34}	2.7×10^{-30}	-2.2×10^{-26}	1.1×10^{-22}	-3.2×10^{-19}	7.2×10^{-16}	-1.3×10^{-12}	1.9×10^{-09}	-2.8×10^{-06}	5.5×10^{-04}
$i = 7$	9.5×10^{-35}	-2.1×10^{-30}	1.8×10^{-26}	-7.8×10^{-23}	1.4×10^{-19}	9.9×10^{-17}	-1.0×10^{-12}	2.1×10^{-09}	-3.0×10^{-06}	5.8×10^{-04}
$i = 8$	2.4×10^{-34}	-4.9×10^{-30}	4.0×10^{-26}	-1.6×10^{-22}	3.0×10^{-19}	8.3×10^{-17}	-1.4×10^{-12}	2.7×10^{-09}	-3.3×10^{-06}	6.0×10^{-04}
$i = 9$	2.0×10^{-34}	-3.6×10^{-30}	2.4×10^{-26}	-5.5×10^{-23}	-1.3×10^{-19}	1.1×10^{-15}	-2.9×10^{-12}	3.9×10^{-09}	-3.7×10^{-06}	6.2×10^{-04}
$i = 10$	-1.3×10^{-34}	3.8×10^{-30}	-4.7×10^{-26}	3.2×10^{-22}	-1.3×10^{-18}	3.5×10^{-15}	-5.7×10^{-12}	5.6×10^{-09}	-4.1×10^{-06}	6.2×10^{-04}

(*continued on next page*)

Table 8 (*continued*)

Time step	a_1	a_2	a_3	a_4	a_5	a_6	a_7	a_8	a_9	a_{10}
$i = 11$	-7.3×10^{-34}	1.7×10^{-29}	-1.7×10^{-25}	9.4×10^{-22}	-3.2×10^{-18}	6.9×10^{-15}	-9.4×10^{-12}	7.8×10^{-09}	-4.6×10^{-06}	6.1×10^{-04}
$i = 12$	-1.4×10^{-33}	3.3×10^{-29}	-3.1×10^{-25}	1.6×10^{-21}	-5.3×10^{-18}	1.1×10^{-14}	-1.3×10^{-11}	9.7×10^{-09}	-4.9×10^{-06}	5.7×10^{-04}
$i = 13$	-2.0×10^{-33}	4.5×10^{-29}	-4.2×10^{-25}	2.2×10^{-21}	-6.8×10^{-18}	1.3×10^{-14}	-1.5×10^{-11}	1.1×10^{-08}	-4.9×10^{-06}	5.1×10^{-04}
$i = 14$	-2.2×10^{-33}	4.8×10^{-29}	-4.4×10^{-25}	2.3×10^{-21}	-7.0×10^{-18}	1.3×10^{-14}	-1.5×10^{-11}	1.0×10^{-08}	-4.5×10^{-06}	4.1×10^{-04}
$i = 15$	-1.9×10^{-33}	4.1×10^{-29}	-3.7×10^{-25}	1.9×10^{-21}	-5.8×10^{-18}	1.1×10^{-14}	-1.2×10^{-11}	7.8×10^{-09}	-3.7×10^{-06}	3.1×10^{-04}
$i = 16$	-1.3×10^{-33}	2.7×10^{-29}	-2.5×10^{-25}	1.2×10^{-21}	-3.7×10^{-18}	6.8×10^{-15}	-7.5×10^{-12}	4.8×10^{-09}	-2.8×10^{-06}	2.1×10^{-04}
$i = 17$	-4.6×10^{-34}	9.8×10^{-30}	-8.8×10^{-26}	4.4×10^{-22}	-1.3×10^{-18}	2.5×10^{-15}	-2.9×10^{-12}	2.1×10^{-09}	-2.0×10^{-06}	1.5×10^{-04}
$i = 18$	-1.4×10^{-34}	3.1×10^{-30}	-3.1×10^{-26}	1.7×10^{-22}	-5.8×10^{-19}	1.3×10^{-15}	-1.7×10^{-12}	1.4×10^{-09}	-1.8×10^{-06}	1.5×10^{-04}
$i = 19$	-2.5×10^{-34}	5.8×10^{-30}	-5.8×10^{-26}	3.2×10^{-22}	-1.1×10^{-18}	2.2×10^{-15}	-2.9×10^{-12}	2.2×10^{-09}	-2.1×10^{-06}	2.1×10^{-04}
$i = 20$	-2.4×10^{-34}	5.7×10^{-30}	-5.6×10^{-26}	3.1×10^{-22}	-1.0×10^{-18}	2.1×10^{-15}	-2.6×10^{-12}	2.0×10^{-09}	-2.1×10^{-06}	2.7×10^{-04}
$i = 21$	-4.0×10^{-34}	8.7×10^{-30}	-8.0×10^{-26}	4.0×10^{-22}	-1.2×10^{-18}	2.2×10^{-15}	-2.5×10^{-12}	1.8×10^{-09}	-2.1×10^{-06}	3.2×10^{-04}

Table 9
Constant coefficients of the polynomial function with degree $n = 9$ in terms of the backward motion

Time step	a_1	a_2	a_3	a_4	a_5	a_6	a_7	a_8	a_9	a_{10}
$i = 1$	1.4×10^{-33}	-2.8×10^{-29}	2.3×10^{-25}	1.0×10^{-21}	2.7×10^{-18}	4.4×10^{-15}	4.3×10^{-12}	-2.5×10^{-09}	4.9×10^{-06}	-3.2×10^{-04}
$i = 2$	8.5×10^{-34}	-1.7×10^{-29}	1.4×10^{-25}	-6.2×10^{-22}	1.7×10^{-18}	-2.9×10^{-15}	3.2×10^{-12}	-2.1×10^{-09}	4.9×10^{-06}	-3.8×10^{-04}
$i = 3$	9.0×10^{-34}	-1.7×10^{-29}	1.4×10^{-25}	-6.5×10^{-22}	1.8×10^{-18}	-3.2×10^{-15}	3.5×10^{-12}	-2.4×10^{-09}	5.0×10^{-06}	-4.4×10^{-04}
$i = 4$	7.7×10^{-34}	-1.6×10^{-29}	1.4×10^{-25}	-6.8×10^{-22}	2.0×10^{-18}	-3.7×10^{-15}	4.2×10^{-12}	-2.8×10^{-09}	5.2×10^{-06}	-5.0×10^{-04}
$i = 5$	1.2×10^{-33}	-2.4×10^{-29}	2.1×10^{-25}	-1.0×10^{-21}	3.0×10^{-18}	-5.3×10^{-15}	5.7×10^{-12}	-3.7×10^{-09}	5.5×10^{-06}	-5.6×10^{-04}
$i = 6$	2.1×10^{-33}	-4.2×10^{-29}	3.6×10^{-25}	-1.7×10^{-21}	4.6×10^{-18}	-7.8×10^{-15}	7.9×10^{-12}	-4.7×10^{-09}	5.8×10^{-06}	-6.0×10^{-04}
$i = 7$	3.5×10^{-33}	-6.8×10^{-29}	5.6×10^{-25}	-2.5×10^{-21}	6.8×10^{-18}	-1.1×10^{-14}	1.0×10^{-11}	-5.7×10^{-09}	6.1×10^{-06}	-6.3×10^{-04}
$i = 8$	4.3×10^{-33}	-8.4×10^{-29}	6.7×10^{-25}	-2.9×10^{-21}	7.6×10^{-18}	-1.2×10^{-14}	1.1×10^{-11}	-5.8×10^{-09}	6.2×10^{-06}	-6.4×10^{-04}
$i = 9$	3.4×10^{-33}	-6.4×10^{-29}	5.0×10^{-25}	-2.1×10^{-21}	5.3×10^{-18}	-8.0×10^{-15}	7.3×10^{-12}	-4.6×10^{-09}	6.2×10^{-06}	-6.3×10^{-04}
$i = 10$	1.1×10^{-33}	-2.1×10^{-29}	1.6×10^{-25}	-6.5×10^{-22}	1.6×10^{-18}	-2.7×10^{-15}	3.4×10^{-12}	-3.4×10^{-09}	6.2×10^{-06}	-6.1×10^{-04}
$i = 11$	-4.2×10^{-34}	7.5×10^{-30}	-5.2×10^{-26}	1.6×10^{-22}	-6.0×10^{-20}	-9.5×10^{-16}	2.9×10^{-12}	-3.9×10^{-09}	6.5×10^{-06}	-5.9×10^{-04}
$i = 12$	4.7×10^{-34}	-1.2×10^{-29}	1.2×10^{-25}	-7.2×10^{-22}	2.6×10^{-18}	-5.7×10^{-15}	8.0×10^{-12}	-6.8×10^{-09}	7.1×10^{-06}	-5.6×10^{-04}
$i = 13$	3.4×10^{-33}	-7.0×10^{-29}	6.0×10^{-25}	-2.8×10^{-21}	8.1×10^{-18}	-1.4×10^{-14}	1.6×10^{-11}	-1.0×10^{-08}	7.7×10^{-06}	-5.0×10^{-04}
$i = 14$	6.2×10^{-33}	-1.2×10^{-28}	1.0×10^{-24}	-4.6×10^{-21}	1.3×10^{-17}	-2.1×10^{-14}	2.1×10^{-11}	-1.2×10^{-08}	7.7×10^{-06}	-4.1×10^{-04}
$i = 15$	6.2×10^{-33}	-1.2×10^{-28}	9.9×10^{-25}	-4.4×10^{-21}	1.2×10^{-17}	-1.9×10^{-14}	1.9×10^{-11}	-1.0×10^{-08}	6.9×10^{-06}	-2.8×10^{-04}
$i = 16$	3.3×10^{-33}	-6.5×10^{-29}	5.3×10^{-25}	-2.4×10^{-21}	6.3×10^{-18}	-1.0×10^{-14}	9.9×10^{-12}	-5.5×10^{-09}	5.6×10^{-06}	-1.5×10^{-04}
$i = 17$	9.9×10^{-34}	-1.9×10^{-29}	1.6×10^{-25}	-7.3×10^{-22}	2.0×10^{-18}	-3.4×10^{-15}	3.6×10^{-12}	-2.3×10^{-09}	4.7×10^{-06}	-9.5×10^{-05}
$i = 18$	1.5×10^{-33}	-3.0×10^{-29}	2.5×10^{-25}	-1.1×10^{-21}	3.1×10^{-18}	-5.2×10^{-15}	5.3×10^{-12}	-3.2×10^{-09}	5.0×10^{-06}	-1.5×10^{-04}
$i = 19$	7.1×10^{-34}	-1.4×10^{-29}	1.2×10^{-25}	-5.9×10^{-22}	1.7×10^{-18}	-3.1×10^{-15}	3.4×10^{-12}	-2.4×10^{-09}	4.9×10^{-06}	-2.0×10^{-04}
$i = 20$	1.6×10^{-33}	-3.0×10^{-29}	2.5×10^{-25}	-1.1×10^{-21}	2.8×10^{-18}	-4.3×10^{-15}	4.1×10^{-12}	-2.4×10^{-09}	4.8×10^{-06}	-2.6×10^{-04}
$i = 21$	1.4×10^{-33}	-2.8×10^{-29}	2.3×10^{-25}	-1.0×10^{-21}	2.7×10^{-18}	-4.4×10^{-15}	4.3×10^{-12}	-2.5×10^{-09}	4.9×10^{-06}	-3.2×10^{-04}

Appendix D. Supplementary data

Supplementary data to this article can be found online at https://doi.org/10.1016/j.ijnonlinmec.2025.105098.

Data availability

Data will be made available on request.

References

[1] J.J. Coy, R.F. Handschuh, D.G. Lewicki, R.G. Huff, E.A. Krejsa, A.M. Karchmer, Identification and proposed control of helicopter transmission noise at the source. https://ntrs.nasa.gov/citations/19870007383, 1987.

[2] X. Dai, C.G. Cooley, R.G. Parker, An efficient hybrid analytical-computational method for nonlinear vibration of spur gear pairs, J. Vib. Acoust. 141 (1) (2018), https://doi.org/10.1115/1.4040674.

[3] F.S. Samani, M. Salajegheh, M. Molaie, Nonlinear vibration of the spiral bevel gear under periodic torque considering multiple elastic deformation evaluations due to different bearing supports, SN Appl. Sci. 3 (9) (2021), https://doi.org/10.1007/s42452-021-04755-6.

[4] M. Molaie, S. Deylaghian, G. Iarriccio, F.S. Samani, A. Zippo, F. Pellicano, Planet load-sharing and phasing, Machines 10 (8) (2022), https://doi.org/10.3390/machines10080634.

[5] M. Molaie, F.S. Samani, F. Pellicano, Spiral bevel gears nonlinear vibration having radial and axial misalignments effects, Vibrations 4 (3) (2021) 666–678, https://doi.org/10.3390/vibration4030037.

[6] M. Molaie, F.S. Samani, H. Motahar, Nonlinear vibration of crowned gear pairs considering the effect of Hertzian contact stiffness, SN Appl. Sci. 1 (5) (2019), https://doi.org/10.1007/s42452-019-0439-y.

[7] H. Motahar, F.S. Samani, M. Molaie, Nonlinear vibration of the bevel gear with teeth profile modification, Nonlinear Dyn. 83 (4) (2016) 1875–1884, https://doi.org/10.1007/s11071-015-2452-z.

[8] J. Wang, H. Wang, L. Guo, Analysis of effect of random perturbation on dynamic response of gear transmission system, Chaos Solitons Fractals 68 (2014) 78–88, https://doi.org/10.1016/j.chaos.2014.08.004.

[9] J.D.M. Marafona, P.M.T. Marques, R.C. Martins, J.H.O. Seabra, Mesh stiffness models for cylindrical gears: a detailed review, Mech. Mach. Theor. 166 (2021), https://doi.org/10.1016/j.mechmachtheory.2021.104472.

[10] A. Kahraman, R. Singh, Interactions between time-varying mesh stiffness and clearance non-linearities in a geared system, J. Sound Vib. 146 (1) (1991) 135–156, https://doi.org/10.1016/0022-460X(91)90527-Q.

[11] T. Eritenel, R.G. Parker, Nonlinear vibration of gears with tooth surface modifications, J. Vib. Acoust. 135 (2013), https://doi.org/10.1115/1.4023913.

[12] C.G. Cooley, C. Liu, X. Dai, R.G. Parker, Gear tooth mesh stiffness: a comparison of calculation approaches, Mech. Mach. Theor. 105 (2016) 540–553, https://doi.org/10.1016/j.mechmachtheory.2016.07.021.

[13] K. De Brabanter, P. Karsmakers, F. Ojeda, C. Alzate, J. De Brabanter, K. Pelckmans, B. De Moor, J. Vandewalle, J.A. Suykens, LS-SVMlab Toolbox User's Guide, Katholieke Universiteit Leuven, 2010, version 1.7. https://www.diva-portal.org/smash/get/diva2:386413/FULLTEXT01.pdf.

[14] L. Gelman, N.H. Chandra, R. Kurosz, F. Pellicano, M. Barbieri, A. Zippo, Novel spectral kurtosis technology for adaptive vibration condition monitoring of multi-stage gearboxes, Insight - Non-Destructive Testing and Condition Monitoring 58 (8) (2016) 409–416, https://doi.org/10.1784/insi.2016.58.8.409.

[15] C.L. Webber, N. Marwan, Recurrence Quantification Analysis: Theory and Best Practices, Springer International Publishing, 2015, https://doi.org/10.1007/978-3-319-07155-8.

[16] M. Molaie, F.S. Samani, A. Zippo, G. Iarriccio, F. Pellicano, Spiral bevel gears: bifurcation and chaos analyses of pure torsional system, Chaos Solitons Fractals 177 (2023), https://doi.org/10.1016/j.chaos.2023.114179.

[17] M. Molaie, F.S. Samani, A. Zippo, F. Pellicano, Spiral Bevel Gears: nonlinear dynamic model based on accurate static stiffness evaluation, J. Sound Vib. 544 (2023), https://doi.org/10.1016/j.jsv.2022.117395.

[18] F. Pellicano, M. Barbieri, A. Zippo, M. Strozzi, Experiments on shells under base excitation, J. Sound Vib. 369 (2016) 209–227, https://doi.org/10.1016/j.jsv.2015.12.033.

[19] A. Zippo, M. Barbieri, G. Iarriccio, F. Pellicano, Nonlinear vibrations of circular cylindrical shells with thermal effects: an experimental study, Nonlinear Dyn. 99 (1) (2020) 373–391, https://doi.org/10.1007/s11071-018-04753-1.

[20] J.P. Eckmann, S.O. Kamphorst, D. Ruelle, Recurrence plots of dynamical systems, World Scientific Series on Nonlinear Science Series A 16 (1995) 441–446.

[21] N. Marwan, J. Kurths, Nonlinear analysis of bivariate data with cross recurrence plots, Phys. Lett. 302 (5) (2002) 299–307, https://doi.org/10.1016/S0375-9601(02)01170-2.

[22] J. Kurths, U. Schwarz, C.P. Sonett, U. Parlitz, Testing for nonlinearity in radiocarbon data, Nonlinear Process Geophys. 1 (1) (1994) 72–76, https://doi.org/10.5194/npg-1-72-1994.

[23] M. Thiel, M.C. Romano, J. Kurths, Analytical description of Recurrence Plots of white noise and chaotic processes, arXiv, (2003), https://doi.org/10.48550/arXiv.nlin/0301027.

[24] L. Borkowski, A. Stefanski, FFT bifurcation analysis of routes to chaos via quasiperiodic solutions, Math. Probl Eng. (2015), https://doi.org/10.1155/2015/367036.

[25] L.S. McCue, A.W. Troesch, Use of Lyapunov exponents to predict chaotic vessel motions, in: Contemporary Ideas on Ship Stability and Capsizing in Waves, Springer, 2011, pp. 415–432, https://doi.org/10.1007/978-94-007-1482-3_23.

[26] A. Wolf, J.B. Swift, H.L. Swinney, J.A. Vastano, Determining Lyapunov exponents from a time series, Phys. Nonlinear Phenom. 16 (3) (1985) 285–317, https://doi.org/10.1016/0167-2789(85)90011-9.

[27] V.K. Tamminana, A. Kahraman, S. Vijayakar, A study of the relationship between the dynamic factors and the dynamic transmission error of spur gear pairs, J. Mech. Des. 129 (1) (2006) 75–84, https://doi.org/10.1115/1.2359470.

[28] X. Sun, Y. Zhao, M. Liu, Y. Liu, On dynamic mesh force evaluation of spiral bevel gears, Shock Vib. (2019) 1–26, https://doi.org/10.1155/2019/5614574, 2019.

[29] M. Abruzzo, M. Beghini, C. Santus, F. Presicce, A dynamic model combining the average and the local meshing stiffnesses and based on the static transmission error for spur gears with profile modification, Mech. Mach. Theor. 180 (2023), https://doi.org/10.1016/j.mechmachtheory.2022.105139.

[30] R.F. Handschuh, G.D. Bibel, Comparison of Experimental and Analytical Tooth Bending Stress of Aerospace Spiral Bevel Gears, Army research inst for the behavioral and social Sciences alexandria va, 1999.

[31] G.D. Bibel, K. Tiku, A. Kumar, Prediction of contact path and load sharing in spiral bevel gears, Report No.: NAS 1.26, https://ntrs.nasa.gov/citations/19940029642, 1994.

[32] F.S. Samani, M. Molaie, F. Pellicano, Nonlinear vibration of the spiral bevel gear with a novel tooth surface modification method, Meccanica 54 (7) (2019) 1071–1081, https://doi.org/10.1007/s11012-019-00973-w.

[33] A. Kahraman, R. Singh, Non-linear dynamics of a spur gear pair, J. Sound Vib. 142 (1) (1990) 49–75, https://doi.org/10.1016/0022-460X(90)90582-K.

[34] G. Liu, R.G. Parker, Nonlinear dynamics of idler gear systems, Nonlinear Dyn. 53 (4) (2008) 345–367, https://doi.org/10.1007/s11071-007-9317-z.

[35] A. Al-shyyab, A. Kahraman, Non-linear dynamic analysis of a multi-mesh gear train using multi-term harmonic balance method: sub-harmonic motions, J. Sound Vib. 279 (1) (2005) 417–451, https://doi.org/10.1016/j.jsv.2003.11.029.

[36] X. Qianfan, Noise, vibration, and harshness (NVH) in diesel engine system design. Diesel Engine System Design, Woodhead Publishing Limited, 2013, pp. 759–821, https://doi.org/10.1533/9780857090836.3.759.

[37] A.C.L. Chian, W.M. Santana, E.L. Rempel, F.A. Borotto, T. Hada, Y. Kamide, Chaos in driven Alfvén systems: unstable periodic orbits and chaotic saddles, Nonlinear Process Geophys. 14 (1) (2007) 17–29, https://doi.org/10.5194/npg-14-17-2007.

[38] C. Grebogi, E. Ott, J.A. Yorke, Chaotic attractors in crisis, Phys. Rev. Lett. 48 (22) (1982) 1507–1510, https://doi.org/10.1103/PhysRevLett.48.1507.

[39] C. Grebogi, E. Ott, J.A. Yorke, Crises, sudden changes in chaotic attractors, and transient chaos, Phys. Nonlinear Phenom. 7 (1) (1983) 181–200, https://doi.org/10.1016/0167-2789(83)90126-4.

[40] J.C. Sprott, Chaos and Time-Series Analysis, Oxford University Press, 2003, https://doi.org/10.1093/oso/9780198508397.001.0001.

[41] L. Zhu, A. Raghu, Y.C. Lai, Experimental observation of superpersistent chaotic transients, Phys. Rev. Lett. 86 (18) (2001) 4017–4020, https://doi.org/10.1103/PhysRevLett.86.4017.

[42] W. Szemplińska-Stupnicka, A. Zubrzycki, E. Tyrkiel, Properties of chaotic and regular boundary crisis in dissipative driven nonlinear oscillators, Nonlinear Dyn. 19 (1) (1999) 19–36, https://doi.org/10.1023/A:1008339214577.

[43] J.F. Mason, P.T. Piiroinen, Interactions between global and grazing bifurcations in an impacting system, Chaos: An Interdisciplinary Journal of Nonlinear Science 21 (1) (2011), https://doi.org/10.1063/1.3551502.

[44] X. Yue, W. Xu, L. Wang, Global analysis of boundary and interior crises in an elastic impact oscillator, Commun. Nonlinear Sci. Numer. Simulat. 18 (12) (2013) 3567–3574, https://doi.org/10.1016/j.cnsns.2013.05.017.

[45] A. Witt, U. Feudel, A. Pikovsky, Birth of strange nonchaotic attractors due to interior crisis, Phys. Nonlinear Phenom. 109 (1) (1997) 180–190, https://doi.org/10.1016/S0167-2789(97)00168-1.

[46] R.H. Abraham, Chaostrophes, intermittency, and noise, chaos, Fractals, and Dynamics (1985), https://doi.org/10.1201/9781003072676-2.

[47] J.M.T. Thompson, H.B. Stewart, Nonlinear Dynamics and Chaos, John Wiley & Sons, 2002.

[48] R. Lidl, Papers in algebra, analysis and statistics, Contemp. Math. (1982) 418, https://doi.org/10.1090/CONM/009.

[49] J.P. Eckmann, D. Ruelle, Ergodic theory of chaos and strange attractors, Rev. Mod. Phys. 57 (3) (1985) 617–656, https://doi.org/10.1103/RevModPhys.57.617.

[50] M.B. Kennel, R. Brown, H.D.I. Abarbanel, Determining embedding dimension for phase-space reconstruction using a geometrical construction, Phys. Rev. 45 (6) (1992) 3403–3411, https://doi.org/10.1103/PhysRevA.45.3403.

[51] V. Deshmukh, R. Meikle, E. Bradley, J.D. Meiss, J. Garland, Using scaling-region distributions to select embedding parameters, Phys. Nonlinear Phenom. 446 (2023), https://doi.org/10.1016/j.physd.2023.133674.

[52] R. Hegger, H. Kantz, T. Schreiber, Practical implementation of nonlinear time series methods: the TISEAN package, Chaos: An Interdisciplinary Journal of Nonlinear Science 9 (2) (1999) 413–435, https://doi.org/10.1063/1.166424.

[53] M.J. Feigenbaum, Quantitative universality for a class of nonlinear transformations, J. Stat. Phys. 19 (1) (1978) 25–52, https://doi.org/10.1007/BF01020332.
[54] M.J. Feigenbaum, The universal metric properties of nonlinear transformations, J. Stat. Phys. 21 (6) (1979) 669–706, https://doi.org/10.1007/BF01107909.
[55] P. Cvitanović, Universality in Chaos, second ed., Routledge, 1989. https://www.routledge.com/Universality-in-Chaos-2nd-edition/Cvitanovic/p/book/9780852742600.
[56] S. Partha, S.H. Strogatz, The birth of period three, Math. Mag. (1995), https://doi.org/10.2307/2691376.
[57] E. Knobloch, N.O. Weiss, Bifurcations in a model of magnetoconvection, Phys. Nonlinear Phenom. 9 (3) (1983) 379–407, https://doi.org/10.1016/0167-2789(83)90279-8.
[58] P.J. Myrberg, Sur l'itération des polynomes réels quadratiques, J. Math. Pure Appl. 41 (9) (1962) 339–351.
[59] E. Sander, J.A. Yorke, Connecting period-doubling cascades to chaos, International Journal of Bifurcation and Chaos 22 (2) (2012), https://doi.org/10.1142/S0218127412500228.
[60] H. Poincaré, Sur le problème des trois corps et les équations de la dynamique, Acta Math. 13 (1) (1890) A3–A270.
[61] W. Feller, An Introduction to Probability Theory and its Applications, John Wiley & Sons, 1991.
[62] N. Marwan, C.L. Webber, Recurrence Quantification Analysis: Theory and Best Practices, Springer International Publishing, Cham, 2015, pp. 3–43, https://doi.org/10.1007/978-3-319-07155-8_1.
[63] N. Marwan, M. Carmen Romano, M. Thiel, J. Kurths, Recurrence plots for the analysis of complex systems, Phys. Rep. 438 (5) (2007) 237–329, https://doi.org/10.1016/j.physrep.2006.11.001.
[64] N. Marwan, Encounters with neighbours: current developments of concepts based on recurrence plots and their applications, PhD Thesis, University of Potsdam, Potsdam (2003). https://nbn-resolving.org/urn:nbn:de:kobv:517-0000856.
[65] H. Kantz, T. Schreiber, Nonlinear Time Series Analysis, Cambridge University Press, 2004, https://doi.org/10.1017/CBO9780511755798.
[66] L. Cao, Practical method for determining the minimum embedding dimension of a scalar time series, Phys. Nonlinear Phenom. 110 (1) (1997) 43–50, https://doi.org/10.1016/S0167-2789(97)00118-8.
[67] M. Thiel, M.C. Romano, J. Kurths, Spurious structures in recurrence plots induced by embedding, Nonlinear Dyn. 44 (1) (2006) 299–305, https://doi.org/10.1007/s11071-006-2010-9.
[68] T.K. March, S.C. Chapman, R.O. Dendy, Recurrence plot statistics and the effect of embedding, Phys. Nonlinear Phenom. 200 (1) (2005) 171–184, https://doi.org/10.1016/j.physd.2004.11.002.
[69] G.M. Mindlin, R. Gilmore, Topological analysis and synthesis of chaotic time series, Phys. Nonlinear Phenom. 58 (1) (1992) 229–242, https://doi.org/10.1016/0167-2789(92)90111-Y.
[70] M. Koebbe, G. Mayer-Kress, Use of recurrence plots in the analysis of time-series data, in: Santa Fe Institute Studies in the Sciences of Complexity-Proceedings Volume, 1992, 361–361.
[71] J.P. Zbilut, C.L. Webber, Embeddings and delays as derived from quantification of recurrence plots, Phys. Lett. 171 (3) (1992) 199–203, https://doi.org/10.1016/0375-9601(92)90426-M.
[72] J.P. Zbilut, J.M. Zaldivar-Comenges, F. Strozzi, Recurrence quantification based Liapunov exponents for monitoring divergence in experimental data, Phys. Lett. 297 (3) (2002) 173–181, https://doi.org/10.1016/S0375-9601(02)00436-X.
[73] L. Matassini, H. Kantz, J. Hołyst, R. Hegger, Optimizing of recurrence plots for noise reduction, Phys. Rev. 65 (2) (2002), https://doi.org/10.1103/PhysRevE.65.021102.
[74] N. Marwan, N. Wessel, U. Meyerfeldt, A. Schirdewan, J. Kurths, Recurrence-plot-based measures of complexity and their application to heart-rate-variability data, Phys. Rev. 66 (2) (2002), https://doi.org/10.1103/PhysRevE.66.026702.
[75] N. Marwan, J. Kurths, Line structures in recurrence plots, Phys. Lett. 336 (4) (2005) 349–357, https://doi.org/10.1016/j.physleta.2004.12.056.
[76] A. Facchini, H. Kantz, E. Tiezzi, Recurrence plot analysis of nonstationary data: the understanding of curved patterns, Phys. Rev. 72 (2) (2005), https://doi.org/10.1103/PhysRevE.72.021915.
[77] J.B. Gao, Recurrence time statistics for chaotic systems and their applications, Phys. Rev. Lett. 83 (16) (1999) 3178–3181, https://doi.org/10.1103/PhysRevLett.83.3178.
[78] V. Balakrishnan, G. Nicolis, C. Nicolis, Recurrence time statistics in deterministic and stochastic dynamical systems in continuous time: a comparison, Phys. Rev. 61 (3) (2000) 2490–2499, https://doi.org/10.1103/PhysRevE.61.2490.
[79] D.P. Lathrop, E.J. Kostelich, Characterization of an experimental strange attractor by periodic orbits, Phys. Rev. 40 (7) (1989) 4028–4031, https://doi.org/10.1103/PhysRevA.40.4028.
[80] A. Provenzale, L.A. Smith, R. Vio, G. Murante, Distinguishing between low-dimensional dynamics and randomness in measured time series, Phys. Nonlinear Phenom. 58 (1) (1992) 31–49, https://doi.org/10.1016/0167-2789(92)90100-2.
[81] C. Rieke, K. Sternickel, R.G. Andrzejak, C.E. Elger, P. David, K. Lehnertz, Measuring nonstationarity by analyzing the loss of recurrence in dynamical systems, Phys. Rev. Lett. 88 (24) (2002), https://doi.org/10.1103/PhysRevLett.88.244102.
[82] J.P. Zbilut, C.L. Webber, Recurrence quantification analysis: introduction and historical context, International Journal of Bifurcation and Chaos 17 (10) (2007) 3477–3481, https://doi.org/10.1142/S0218127407019238.
[83] C.L. Webber, J.P. Zbilut, Dynamical assessment of physiological systems and states using recurrence plot strategies, J. Appl. Physiol. 76 (2) (1994) 965–973, https://doi.org/10.1152/jappl.1994.76.2.965.
[84] L.L. Trulla, A. Giuliani, J.P. Zbilut, C.L. Webber, Recurrence quantification analysis of the logistic equation with transients, Phys. Lett. 223 (4) (1996) 255–260, https://doi.org/10.1016/S0375-9601(96)00741-4.
[85] C.L. Webber Jr., J.P. Zbilut, Recurrence quantification analysis of nonlinear dynamical systems, Tutorials in contemporary nonlinear methods for the behavioral sciences 94 (2005) 26–94.
[86] Y. Chen, H. Yang, Multiscale recurrence analysis of long-term nonlinear and nonstationary time series, Chaos, Solitons & Fractals 45 (7) (2012) 978–987, https://doi.org/10.1016/j.chaos.2012.03.013.
[87] N. Marwan, TCross recurrence plot toolbox for MATLAB®. https://tocsy.pik-potsdam.de/CRPtoolbox/, 2024.
[88] H. Yang, Multiscale recurrence quantification analysis of spatial cardiac vectorcardiogram signals, IEEE (Inst. Electr. Electron. Eng.) Trans. Biomed. Eng. 58 (2) (2011) 339–347, https://doi.org/10.1109/TBME.2010.2063704.